35

SATELLITE & MESOMETEOROLOGY
RESEARCH PROJECT

Department of the Geophysical Sciences
The University of Chicago

SYNOPTIC STUDY OF COLD AIR OUTBREAK OVER THE MEDITERRANEAN USING SATELLITE PHOTOGRAPHS AND RADIATION DATA

by

Aasmund Rabbe and Tetsuya Fujita

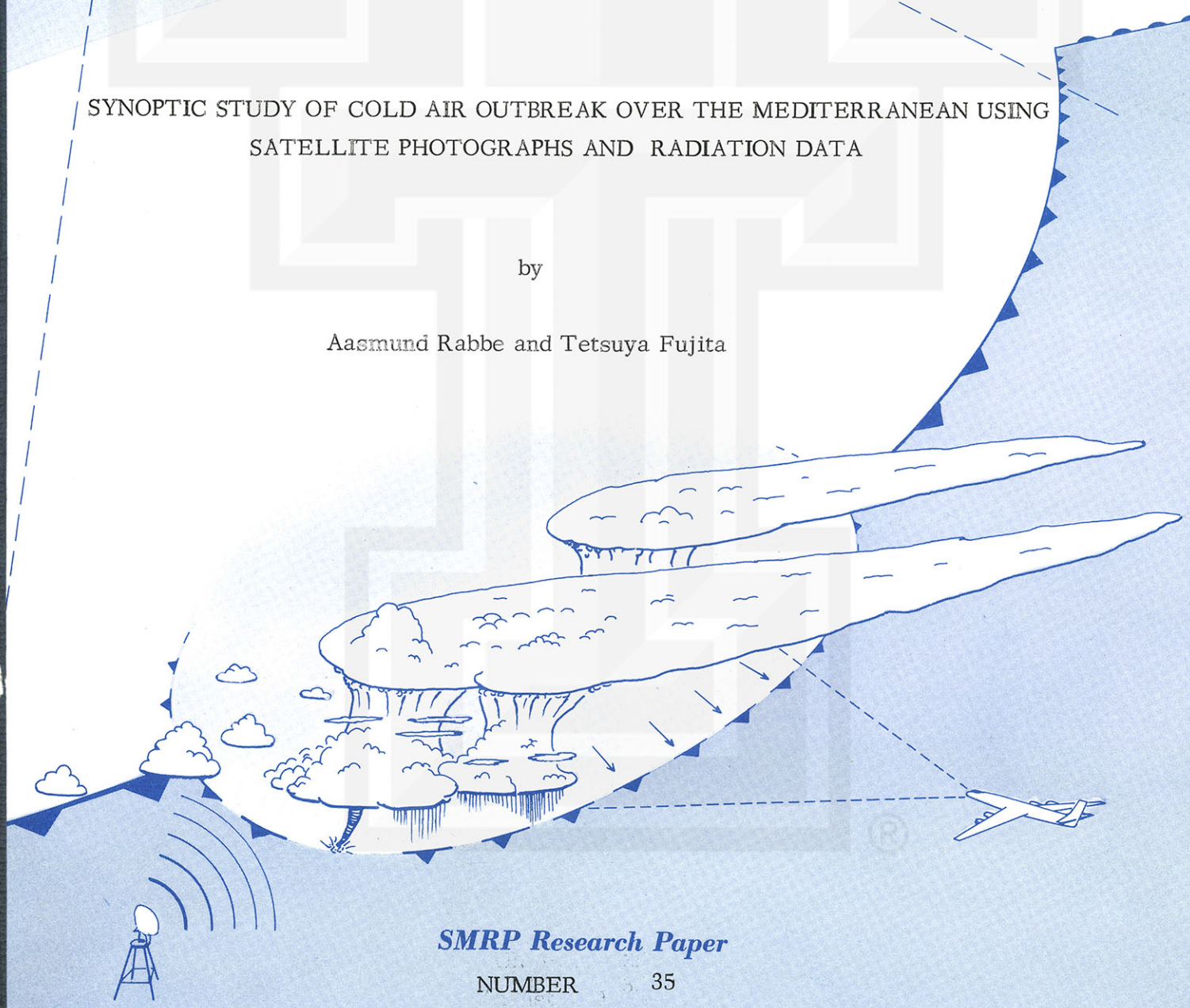

SMRP Research Paper
NUMBER 35
August 1964

MESOMETEOROLOGY PROJECT ---- RESEARCH PAPERS

1.* Report on the Chicago Tornado of March 4, 1961 - Rodger A. Brown and Tetsuya Fujita

2.* Index to the NSSP Surface Network - Tetsuya Fujita

3.* Outline of a Technique for Precise Rectification of Satellite Cloud Photographs - Tetsuya Fujita

4.* Horizontal Structure of Mountain Winds - Henry A. Brown

5.* An Investigation of Developmental Processes of the Wake Depression Through Excess Pressure Analysis of Nocturnal Showers - Joseph L. Goldman

6.* Precipitation in the 1960 Flagstaff Mesometeorological Network - Kenneth A. Styber

7.** On a Method of Single- and Dual-Image Photogrammetry of Panoramic Aerial Photographs - Tetsuya Fujita

8. A Review of Researches on Analytical Mesometeorology - Tetsuya Fujita

9. Meteorological Interpretations of Convective Nephsystems Appearing in TIROS Cloud Photographs - Tetsuya Fujita, Toshimitsu Ushijima, William A. Hass, and George T. Dellert, Jr.

10. Study of the Development of Prefrontal Squall-Systems Using NSSP Network Data - Joseph L. Goldman

11. Analysis of Selected Aircraft Data from NSSP Operation, 1962 - Tetsuya Fujita

12. Study of a Long Condensation Trail Photographed by TIROS I - Toshimitsu Ushijima

13. A Technique for Precise Analysis of Satellite Data; Volume I - Photogrammetry (Published as MSL Report No. 14) - Tetsuya Fujita

14. Investigation of a Summer Jet Stream Using TIROS and Aerological Data - Kozo Ninomiya

15. Outline of a Theory and Examples for Precise Analysis of Satellite Radiation Data - Tetsuya Fujita

* Out of print

** To be published

(Continued on back cover)

SATELLITE AND MESOMETEOROLOGY RESEARCH PROJECT

Department of the Geophysical Sciences

The University of Chicago

SYNOPTIC STUDY OF COLD AIR OUTBREAK OVER THE MEDITERRANEAN USING SATELLITE PHOTOGRAPHS AND RADIATION DATA

by

Aasmund Rabbe and Tetsuya Fujita

SMRP Research Paper #35

August 1964

The research reported in this paper has been supported by the National Aeronautics and Space Administration under grant NASA NsG 333 and by the National Weather Satellite Center, U.S. Weather Bureau, under grant CWB WBG - 6.

SYNOPTIC STUDY OF COLD AIR OUTBREAK OVER THE MEDITERRANEAN USING SATELLITE PHOTOGRAPHS AND RADIATION DATA

Aasmund Rabbe and Tetsuya Fujita

Department of the Geophysical Sciences

The University of Chicago

Chicago, Illinois

ABSTRACT

Pictures and radiation data from three orbits of TIROS IV have been used in this paper to interpret the synoptic situation in connection with a cold air outbreak over the Mediterranean. Computations of divergence and vertical velocity have been made and compared with the cloud distribution obtained from the satellite photographs. Both radiation and synoptic patterns are analyzed on sigma-t charts on which the longitude and latitude lines are distorted.

1. Introduction

Satellite pictures and radiation data have been used in several studies of synoptic features, such as cloud distribution, surface temperatures, and cloud top temperatures. Fritz and Winston (1961), and Pedersen and Fujita (1963) found that Channel 2 (8μ - 12μ) data can be used in detecting large-scale overcast areas during both day and night. Cloud heights can be estimated within a limit of several thousand feet depending on cloud structures and areas. Wark et al. (1962) used the same channel in an attempt to find surface temperatures, by correcting for water vapor content and ozone, and found good agreement with the shelter temperatures. Nordberg, Bandeen, et al. (1962) have utilized all five Channels from TIROS III. Although their temperature calculations from Channel 2 are not as promising as those by Wark et al., they found good agreement in the amount of reflection for similar surfaces in all three

cases they studied. Fritz et al. (1964) have made use of Channel 3 (0.25μ - 6.0μ) to compute the earth's albedo; their results imply that the albedo obtained by a satellite is smaller than previously obtained by other methods. The main reason for this is the degradation of the sensor after launch.

Most of these earlier studies have been quite restricted in detail by the sampling interval of the computer in the radiation tape. With the development of Fujita's (1964) scanning printer the radiation analog traces can be read off and printed in detail making it possible to present radiation maps with about seven times as many data points at exact position as those included in FMRT listings.

The purpose of this study is to show how satellite radiation data and photographs can be used to interpret a synoptic situation. The area of analysis shown in Fig. 1 covers the Mediterranean. The figure also includes the subpoint tracks of TIROS IV Orbits 85 R/O 86, 99 R/O 100, and 113 R/O 114 on 14, 15, and 16 February 1962, respectively. The time of these satellite passes over the Mediterranean was in the daylight hours, thus making it possible to use radiation data from both Channels 2 and 3.

The Mediterranean region is a rather interesting area to work on because of its wide variety of topography and surface conditions, i.e.,mountain, sea, island, desert, etc., which can be used in studying their radiative characteristics.

2. The Synoptic Situation

The 1200GMT surface weather maps were closest in time to the selected satellite passes. Data were obtained from the Northern Hemisphere Tabulations and supplemented by additional data from Turkey, Egypt, Libya, and Greece. These were plotted on special distorted maps (see Section 4), using mesosynoptic symbols presented by Fujita et al. (1962). In these symbols, the low cloud cover is distinguished from the total cover (Fig. 2). The available surface data were insufficient for most of the area except for Egypt, Libya, and Turkey; however, they are dense enough to study radiation data in relation to the synoptic situations.

The weather situation during this period was dominated by a cold outbreak from the north into the Mediterranean area. By 1200GMT on 14 February (Fig. 2) the cold

front extended from Tunisia across the Mediterranean Sea east of Malta to Greece. A jet stream with maximum winds of about 100 kts was located over the vicinity of this cold front. The 300-mb contour chart at 0000GMT on 15 February (Fig. 3) shows the existence of another jet stream over Libya and Egypt. The 24-hour temperature changes are about -10C at 700 mb, -15C at 500 mb, and little change at the 300-mb level except for the closed cold core over northern Italy.

The surface map at 1200GMT on 14 February shows an almost solid cloud cover over Egypt. Except for a cumulus cover at Benghazi, the North-African coast is clear from Mersa Matruh west through Tripoli. Along the frontal zone the sky is overcast with some rain over Greece, while over the ocean surface observations are missing. Behind the front the weather is dominated by broken Sc, Cu, and Cb associated with showers. The Tunisian and Algerian coastline from Bizerte to west of Alger shows an almost continuous cloud cover. The French-Italian Riviera is virtually clear; however, Cu and Cb activity appear already at Corsica. Northern Italy is almost clear; in the middle of the country east of the Apennine Mountains there is overcast with scattered rain and snow while the west coast shows a broken cloud cover.

The next day the synoptic situation (Fig. 4) shows almost the same features as the day before. The frontal zone, more or less dissolved except over Turkey, has moved eastward and now extends from the Gulf of Sirte to Crete into Turkey. The low clouds over Egypt have dissipated, thus leaving only Ci and scattered Ac. The coastline from Alexandria to Derna in Libya as well as the inner Gulf of Sirte is still clear, while behind the front there is a continuous Sc and Cu cloud cover to Tripoli. From Tripoli westward to Bizerte the sky is clear due to the lee effect of the Atlas mountain range. The weather in the western Mediterranean shows the same main features as on the previous day, except that the cloud cover has become more broken and scattered.

On 16 February (Fig. 5) the weather situation in the Mediterranean is undergoing some change. The upper air trough has moved eastward and a cold air mass from Russia is pushing southward. Analysis of synoptic data shows that the frontal zone, now stretching from Turkey to the Egyptian coast, has become more active than on the previous day. To the rear of the front there is a broad area with cumulus and cumulonimbus clouds. Egypt is clear except for a narrow band of cirrus clouds which extends from

Cairo to Jerusalem. A prefrontal system accompanied by a solid Sc and As cloud cover has moved in over France. The pressure is rising rapidly over the western Mediterranean and the weather is clearing up here, so that only scattered Sc and Cu remain.

Computations of divergence and vertical velocity were made at 0000GMT on 15 February using the kinematic technique. Streamline and isotach charts were constructed for several levels from 1000 mb up to 200 mb. Since this technique requires extreme accuracy and density of wind observations, the results may be a little doubtful in mountain regions since the mountain influence extends to relatively high levels. However, the computed patterns show a fairly good agreement with the observed weather. Figure 6 represents the computed divergence at the 700-mb level. This level is chosen in order to minimize the influence of the topography. Nevertheless, the great effect of the Alps can still be seen in the divergence field. North of the mountains there is a zone of maximum convergence while on the south side there is a zone of maximum divergence. This divergence zone is rather narrow and runs almost perpendicular to the wind direction. Another convergence zone is located just off the Spanish east coast. Along the northern side of the jet stream over the Mediterranean there is a strong zone of convergence with two maxima, one over Sicily and the other to the east of Greece.

Figure 7 represents the vertical velocity at the 500-mb surface which is close to the level of maximum vertical velocity. It was obtained by

$$\begin{aligned} w_{850} &= w_{1000} + \overline{Div}_{1000}^{850} \cdot \Delta Z_{1000}^{850} \\ w_{700} &= w_{850} + \overline{Div}_{850}^{700} \cdot \Delta Z_{850}^{700} \\ w_{500} &= w_{700} + \overline{Div}_{700}^{500} \cdot \Delta Z_{700}^{500} \end{aligned} \qquad (1)$$

The result thus obtained shows the same main feature as the divergence field; north of the Alps there is a region of strong upward motion while the south side is dominated by strong downward motion. The north side of the jet stream over the Mediterranean is characterized by relatively high upward motion with a maximum over the frontal zone between Greece and Turkey. An area of upward motion off the east coast of Spain may be partly due to a wave effect set off by the Pyrenees. Between the zones of strong downward motion over Yugoslavia and Northern Italy there is an area of weak upward

motion that crosses Italy south of Ancona. The persistent cloud cover over mid-Italy seems to be connected with this area.

3. Analysis of Satellite Pictures

Orbit 99 R/O 100 on 15 February was the only one from which a series of photographs is available. There were 20 usable frames but, due to the high tilt, some pictures show only a small portion of the earth. Most of the frames were, however, utilized in constructing the cloud composite chart shown in Fig. 8. The extensive area of strong divergence south of the Alps and the weaker area in the eastern Mediterranean (Fig. 6) are more or less cloud free. The convergence zone along the north side of the jet stream coincides well with the persistent cloudiness between Sicily and Thessalonica in Greece. The well-defined cloud cover over central Italy coincides with the weak band of convergence over the area. Two bands of broken cloud cover extending from the Gulf of Sirte to Turkey correspond to the frontal zone.

The chart also shows interesting characteristics about the topographic influence on the cloud cover. It is seen that cumuliform clouds which develop on the windward sides of Corsica and Sardinia are blocked by the islands since clear areas extend in the narrow areas where a wake is expected. The orographic effect of the Atlas Mountains shows up in a solid cloud cover.

Three picture frames (Nos. 7, 4, and 1) were selected to show the main features in the cloud cover and some details which would be difficult to pick up otherwise. Frame 7 was taken at 10h 43m 12s (Fig. 9). The satellite position was just east of Sitia in Crete. The tilt was 62.4 deg, and the principal line was pointing WNW. The 500-mb contour lines at 1200GMT were superimposed on the photograph, and it can be seen that the cloud bands in western Mediterranean closely follow these contour lines. It appears that the tops of the clouds between Sicily and Greece have been blown off by the wind. The cloud bands drifting off are not all parallel with the contour lines, which indicates they extend to higher levels than 500 mb. Frame 4 (Fig. 10) was taken at 10h 14m 12s when the TSP was just off the Egyptian coast at Alexandria. The principal line was still directed WNW. Two bands of cloudiness associated with

the frontal system are well-defined in this picture. The open space between them may be a result of lee or corner effect caused by the low Jebel El Akhdar Mountains in Benghazi. One interesting detail shown in this picture is the group of narrow parallel cloud-bands to the northeast of Crete which are aligned at about a 45-deg angle to the main wind direction. The highest mountains in Crete are about 2500 m above sea level, and the cloud bands have the same orientation as the mountain range. The cloud bands must, therefore, be lenticularis or wave clouds formed on the crest of standing mountain waves. The wavelength is approximately 16 km, which is common for standing mountain waves.

Frame 1 (Fig. 11) was taken at 10h 46m 12s, when the exposure subpoint was just east of the Red Sea. In this picture the cloud systems over the western Mediterranean are not very distinct because of the high nadir angle of view. The eastern Mediterranean is mostly clear. The Libyan and Egyptian coastline is well defined and so is the Nile river. The clouds over Egypt, reported from the ground as Ci and Ac, appear to have waves associated with cloud bands normal to the main wind direction. These cannot be mountain waves; however, since the southerly jet stream runs over Egypt, it may be assumed that these clouds are formed on the right hand side of the jet stream core. The wave formation may have been caused by turbulent motion connected with the strong vertical windshear. The wavelength, estimated to be between 15 and 18 km, is unusually long for jet stream wave clouds. However, Schaefer,* who has done considerable work on jet stream clouds, states that he has seen wave clouds associated with jet streams of longer wavelengths than exist in this case. Rather dense cirrus and altocumulus appear to the south of the wave clouds. A long narrow band of cirrus oriented in the direction of the wind appears to be the northern limit of the clouds. In many cases a narrow band of cirrus is observed along the northern limit of such wave clouds (Kuettner, 1959). This picture clearly shows the entire view of both waves and a line of cirrus extending in the direction of the jet stream.

---

* In correspondence with the authors.

4. Radiation Data Analysis

TIROS IV carried a radiometer similar to those used in TIROS II and III - although Channel 4 (7-30 μ) was inoperative. Since this study deals with daytime measurements, all four channels are usable; however, Channels 1 and 5 contained too much noise, which sometimes obscures meteorological signals. To determine the correct time on the radiation tape, nadir angles obtained from the analog traces were compared with the nadir angles computed from OEC charts, using precise spin-axis data. Fujita's scanning-printer was used to print out radiation data. Data from each scan are given along a straight line on a sigma-t printout sheet. Isolines of both scan angles and isochrones are drawn on each printout sheet and OEC chart. By transferring longitude and latitudes from the OEC chart to the printout sheet a longitude and latitude grid which fits the printout sheet was obtained. Because of the conical scanning used in TIROS, the grid lines are distorted considerably, especially near the horizon. After the completion of the grid lines, landmarks are also drawn on the chart. This way of presenting the satellite radiation data seems to be more convenient than transferring the data to a conventionally projected map. In the distorted map one immediately gets the feeling that the data near the horizon are useless due to limb darkening and excessive distortion. If the same data were transferred to a Mercator projection, for example, one would not get the same impression.

The three analyzed orbits begin at almost the same spot over southern France (Fig. 1). The TSP tracks run ESE and the analysis has been discontinued over the Red Sea. The satellite nadir angles over Southern France and Italy are so large that both floor and wall sensors are scanning the earth at the same time (alternating mode). Only the data from the floor sensor, which is facing westward, have been used in this study. After passing over Italy the wall sensor is pointing out in space during the entire spin and only the floor sensor is scanning the earth. Due to the high nadir angles the analyzed sections of the orbits are in an open mode. The first and the second horizons, which limit the scans on the earth, appear here (Fig. 12) as two diverging lines in the direction of motion of the satellite.

Errors in the Radiation Data. There is strong evidence that all channels of medium resolution carried on TIROS IV degraded after going into orbit (NASA, 1963).

The degradation continued until Orbit 600, after which a stable response was maintained. Orbits 85, 99, and 113 occurred during the strongest degradation period and the values obtained from these orbits are, therefore, smaller than they would have been if no degradation had taken place. No corrections have been added to these values, partly because the calibration characteristics of Channel 3 were not completely known, and partly because relative values can be used for the interpretation of the synoptic conditions as well as exact values. As for Channel 2, corrections for water vapor content and ozone have not been made; as a result, the surface temperature computed from Channel 2 will be too low compared with the observed shelter temperature. Limb darkening will also lower the Channel 2 values, especially near the horizon and in the western part of the orbits where the satellite zenith angles are very high. It is evident that the temperature calculations are very sensitive at low energy values, so that small errors in the energy result in large temperature errors (cf. ,the conversion table in Fig. 12).

In case of broken or scattered cloudiness a sensor will measure radiation from both cloud-tops and their background. This factor can be taken into consideration if it is known how large a part of the scan spot is filled by clouds and how large a part is represented by background. Both Channel 2 and Channel 3 must be available in order to estimate the cloud top and the background radiations in case of broken cloud cover. Fujita is working on this problem, and the results will be reported later. It should be kept in mind always that radiation values are more or less doubtful unless the entire field of view is filled with a unique radiant emittance.

Orbit 85, 14 February. Figure 12 shows the effective radiant emittance in watts per square meter measured by Channel 2 (8-12 μ) in Orbit 85.

The synoptic map (Fig. 2) indicates that most of the Libyan coast is clear. Figure 12 on the other hand shows an area of high radiation values over Libya. The value 38 watts/m^2, corresponding to 7C in the table, is seen in this area whereas the reported shelter temperatures are about 20C. Over southern Egypt near Aswan, the radiation values indicate a maximum temperature of 22C. The shelter temperature is 33C and the mixing ratio very low. The differences between calculated temperature from Channel 2 and observed temperature, 13C and 11C respectively, would

be even larger if the shelter temperature were replaced by the soil temperature. The ship reports indicate that the sky over the Mediterranean Sea east of Crete is mostly clear (Fig. 14) and that sea surface temperatures are about 17C. The radiation map indicates a temperature of 1C. The great difference may be caused by the cirrus clouds west of Egypt. There is a relatively clear area over the sea south of the Riviera; the reading from the radiation map is -7C, whereas the actual sea surface temperature is about 14C. In this area the cumulus activity is reported offshore and a part of the scan spot may have been filled with cold cumulus or cumulonimbus clouds. An additional reason for these discrepancies may be the higher humidity over the sea surface. These may explain the large differences between computed and actual temperatures.

The cloud system over Egypt shows up clearly in the radiation map. The lowest temperature in the central part close to the TSP track is -56C, which corresponds to a height of 40,000 ft estimated from the 1200GMT soundings at Mersa Matruh. An aircraft, leaving Cairo at midnight, reported Cs tops at 32,000 ft over the area far to the west of the central cloud mass. Over the frontal zone, between Kirkyra, Greece and Brindisi, Italy, three pilot reports indicate the average cloud top heights to be 30,000 ft. Two of the reports were quite close in time to the satellite pass. The sounding from Athens at 1200GMT registered -47C at 30,000 ft; while the temperature reading from the radiation map is about -45C showing a good agreement with the pilot reports. A cold spot over central Italy, -56C, corresponds to a height of about 33,000 ft where pilot reports give variable heights from 24 to 28,000 ft over the area; the aircraft tracks are, however, some distance to the east of this cold spot. The Pyrenees and the Alps also appear as cold areas in the radiation map. Several cells in the western Mediterranean behind the cold front were measured to be very cold. This result agrees with the synoptic map which indicates intense Cb activity in this area.

Figure 13 is a map of the effective radiance, $\frac{\overline{W}}{\pi}$, or the reflected energy received by Channel 3 measured in watts m^{-2} $sterad^{-1}$, and isolines of incoming extra-terrestrial effective solar radiation, $\frac{\overline{H^* \cos\zeta^*}}{\pi}$, also in watts m^{-2} $sterad^{-1}$. The ratio between these two quantities, $\frac{\overline{W}}{\overline{H^* \cos\zeta^*}}$, where ζ^* denotes the solar zenith angle, represents the reflectance toward a particular direction from which

the value was measured by the satellite. That these values are too low can easily be seen from the map, in which the sea appears completely dark wherever clouds are lacking. One would at least have expected some reflection from the sea surface. It can easily be seen that this map is more capable of clearly distinguishing the differences between the sea surface and the ground than the infrared map. It is interesting to see how sharply the coastlines stand out in this Channel 3 chart along the coast of Libya and at the Riviera where the sky is clear. A knowledge of the ground surface is important in distinguishing between clear and cloud-covered areas. The maximum reflectance of large areas of cloud cover are as follows: over Egypt 68%, over Greece 58%, over Central Italy 55%, and over the Atlas Mountains 50%. In most of these cases the scan spot is filled by a more or less uniform cloud top surface, which accounts for the high reflectance.

From the partly cloudy and snow-covered Alps and Pyrenees Mountains the values are 55% and 46% respectively. One would probably expect higher values from snow and clouds combined, but the scan spot over these mountain areas will not be filled by a uniform reflecting surface. Black mountainsides, for instance, may partly reduce the energy emitted to the satellite unless they are covered with snow or clouds. The two islands, Corsica and Sardinia, coincide with two maximum zones of reflectance, 30% and 44% respectively. Both of these islands have mountains higher than 2,000 meters and the orographic effect on the clouds from these mountains must account for the high response in Channel 3. The elongated area of high reflectance, 44%, between these islands and the Italian west coast is assumed to consist of cumulus or cumulonimbus clouds. In the infrared map (Fig. 12), the same area gives temperatures as low as -50C, which corresponds to a cloud height of about 27,000 ft. This height may probably be too low since this is a case where the background radiation contributed partially to the measured values. West of Benghazi in the Mediterranean Sea the Channel 3 map shows a reflectance of 23%, which means that here exists a partly cloudy area. In the infrared map the same area radiates with a temperature 5C to 10C lower than the surrounding sea. From this one may conclude that the cloud cover consists of low clouds. The synoptic reports from three ships and the Benina weather station on the coast reported broken cumulus covers.

The relatively great variation in the reflectance from the different cloud systems may have several causes. One important variation is that the reflectance values to the south of the TSP track are consistently smaller than the values to the north of the track. This is assumed to depend on the angle between the incident solar beam and the scattered light from the scan spot to the satellite. The relationship is expressed by the equation (Feigelson et al. 1960):

$$J = \int_0^{\pi} \gamma(\phi) \sin\phi \, d\phi \qquad (2)$$

where ϕ is the scattering angle and $\gamma(\phi)$ partly dependent on the pureness of the air. The reflectance from a cloud top will have a maximum value in the forward direction of the incident solar beam, a secondary and smaller maximum in the backward direction, and two minimum values approximately normal to the beam. In this case the scattering angle is varying from 100° in the southern part to about 170° in the northern part, which may explain the apparently larger values to the north of the TSP track.

Orbit 99, 15 February. Infrared radiation from the earth, measured by Channel 2 from Orbit 99, is shown in Fig. 14. The area in Libya close to the Egyptian border is clear as on the day before. The temperature reading in the infrared radiation map from the warmest place is 12C, whereas the shelter temperature is 24C. The difference, 12C, corresponds well with the 13C difference the day before. The higher temperature both in the radiation map and the observed shelter temperature may be due to stronger insolation because the cloud cover over Egypt has mostly dissipated. Near Aswan the infrared radiation temperature is 24C, while the surface shelter temperature is 31C.

The synoptic map and the satellite photographs show a vast clear area in the eastern Mediterranean Sea. Channel 2 temperature readings are about 7C, which is 10C lower than the actual sea surface temperature. The much smaller difference than that of the preceding day must be due to the dissipation of the cloud cover. In the sea south of the Riviera the infrared map gives a maximum temperature of 4C, which also is 10C lower than the actual sea surface temperature. The area is much less cloudy than the day before, which must account for the smaller difference.

The cloud systems in this orbit have already been discussed in detail in the section concerning the satellite photographs and the cloud composite chart. In the infrared map there is no difficulty in recognizing the different cloud systems. It should be noted that all the areas of solid cloud cover show a higher equivalent blackbody temperature than on the preceding day. The lowest temperatures are: over Egypt -24C, over Greece -36C, over Atlas Mountains -27C, and over Central Italy -43C. A flight report gives the top of the wave clouds northeast of Crete as 18,000 ft, which is reasonable. Two flight reports agree on broken Ci at 31,000 ft over western Greece; the corresponding sounding temperature is -54C, while, as we have seen, the infrared temperature is only -36C, which might mean that only a certain portion of the radiation originated at the top of the highest cirrus.

The solid cloud mass over Central Italy seems to be in the same position as on the 14th and the minimum blackbody temperature is -43C. Two aircraft reports indicate continuous cirrostratus over the area at 28,000 and 30,000 ft; these heights correspond to -53C to -55C. If the pilot reports are to be trusted, this indicates that the upper part of the cirrus cloud is more or less transparent allowing radiation from lower parts of the cloud mass to penetrate the upper part. Here again one must realize that small errors in energy values give considerable errors in the temperature readings.

The effective radiance from Orbit 99 is shown in Fig. 15. Isolines for incoming extra-terrestrial effective solar radiation are also drawn on the map. Here it happens again that the clear areas over the sea give no response in Channel 3. The cloud systems over Greece and the Atlas Mountains are reflecting 57% and 51% respectively, which are mainly the same values as those on the preceding day, but the maximum reflecting areas are much smaller. In connection with the clouds over Greece, it should be noted that the maximum zone of reflectance does not coincide with the zone of lowest energy received by Channel 2. It is tempting to construe this as a technical error, but in checking the radiation analog trace it was found that there was a small difference between the times of the lowest energy of Channel 2 and the highest energy of Channel 3. This cloud cover has a steep slope toward southeast and the slope may direct more reflection to the satellite than the highest top of the cloud, while the infrared radiation has its lowest value at this top. The bright cloud over Central Italy,

which is reflecting slightly more than on the previous day, confirms this since the lowest energy in Channel 2 is farther to the west than the brightest reflectance in Channel 3. These examples also show how complicated the reflectance from the earth in different directions can be. The Alps and the Pyrenees give 51% and 44% respectively, a little less than on the 14th. It should be noted that the clouds in the western Mediterranean Sea appear highly reflective in Channel 3, nearly the same as the previous day, while the temperatures in Channel 2 are much higher. The latter fact might indicate that the clouds have changed from cumulonimbus to cumulus and stratocumulus. The synoptic reports are in close agreement with this change. The jet stream clouds over Egypt do not appear so clearly in Channel 3 due to the fact that the background, consisting mostly of sand, reflects almost as intensely as clouds; in Channel 2 the contrast with the surrounding background is much clearer due to the high surface soil temperature.

Orbit 113, 16 February. An infrared radiation map from Orbit 113 is shown in Fig. 16. Again the same area in Libya at the Egyptian border shows a 10-13C lower temperature in Channel 2 than the observed shelter temperature. Near Aswan in southern Egypt the maximum radiation gives an equivalent blackbody temperature of 22C while the maximum shelter temperature in the area is 32C. This time the two maxima do not coincide, which is due apparently to a small error in the map gridding. The error can be checked from the minimum value which coincides with the eastern shoreline of the Red Sea. One would expect this minimum to be in the middle of the sea. From the synoptic map it is known that the clouds over the western Mediterranean are in the process of decaying, and a new frontal system is arriving from the west. In the eastern Mediterranean, cold air from Russia pushing southwards over Turkey and Greece gives new life to the old cold front; all this can be seen in the radiation maps as well. Over the Riviera, Channel 2 registers a very low temperature, down to -63C. The maximum reflectance from this area is a little less than 50%, which indicates the upper clouds consist of diffuse Cs (Fig. 17). The bright cloud which was stationary over Italy during the two previous days is now in rapid deterioration. The reflectance is still 35% but on the infrared map the area shows only a slightly lower temperature than the surroundings. Over the sea between France and Algeria the cloudiness seems to closely follow the main wind direction. This stands out very

clearly in the radiation maps, especially in Channel 3. The cloud cover associated with the cold outbreak from Russia gives high reflectance, 62%, in Channel 3 and low temperature, -50C, in Channel 2. Cells of Cb or thunderstorms can be seen between Greece and Crete with reflectance somewhat less than 50% and a low cloud top temperature around -37C. This temperature corresponds to a cloud height of 20,000 ft; however, seven hours earlier an aircraft reported thunderstorms with continuous Cb and Cs having tops at 27,000 ft.

Over Egypt there is still an elongated cirrus or altocumulus cloud associated with the jet stream. The reflectance of this cloud is 37%, which is about 10% higher than that of the sand dunes to the west. Channel 2 gives a minimum temperature of -23C which contrasts sharply with the surrounding surface temperatures that appear to be about 10C to 15C in the radiation map. Here the cirrus cloud temperature is too high due to the inclusion of background radiation.

Figure 18 shows the relationship of equivalent blackbody temperature, evaluated from the radiation maps, to the observed shelter temperature and to the estimated cloud top temperature. The evaluated surface temperatures are 10C to 12C lower in average than the observed shelter temperatures, mainly because no corrections for water vapor and ozone have been made. The evaluated cloud top temperatures are too high compared with the estimated temperatures. The optical path corrections are much less for these values than for the surface values (Hanel et al. 1962), and in addition radiation from lower parts of the clouds must have reached the satellite sensor.

5. Summary and Conclusion

Satellite pictures, radiation maps, and surface synoptic data correspond remarkably well in this case. The pictures give a very good idea of cloud structure and distribution, especially cirrus bands, cloud streets, and details like mountain waves, etc., which can seldom, if ever, be detected through radiation measurements at the present time. However, many cloud types like stratus, stratocumulus, and altostratus often appear in the pictures without any significant differences. In order to distinguish the difference in cloud heights, radiation maps are very helpful. In

Channel 3, the cloud cover contrasts strongly with the clear areas, except for snow and sand covered surfaces. Especially over sea surfaces can cloudiness be easily detected and outlined if it is of reasonably large dimensions. Channel 3 data provides a good time check since the coastlines and other landmarks stand out very clearly in the map. Channel 2 is able to give information about the surface temperatures. In this case it gives persistently low values because no corrections have been added to the computed values. Under identical meteorological conditions the differences between computed blackbody temperatures and observed shelter temperatures seem to be fairly constant. Cloud top temperatures, evaluated from Channel 2 without any corrections, coincide to a certain extent with estimated cloud top temperatures from pilot reports in cases of solid cloud cover. When the clouds are in a decaying process the cloud top temperature from Channel 2 appears to be too high. This is assumed to be a result of the diffuseness of a decaying cloud which permits radiation from the lower and warmer part of the cloud mass to penetrate the upper part. A growing cloud system seems also to give a relatively higher reflectance than a decaying cloud system. This may be due to the fact that those clouds will have a more uniform and continuous upper surface. By utilizing both Channels 2 and 3 one can more easily distinguish between high and low clouds, and perhaps between the types of clouds. The cloud forms give additional information, like cirrus associated with a jet stream appear as an elongated band, while cumulonimbus shows a more cellular form. Over a sea surface Channel 3 is an excellent cloud detector, but over a sand surface, which is a good reflector, Channel 2 becomes more important in cloud detection. Channel 3 can be used to estimate the earth's albedo, but in doing this one must be aware of how dependent the energy received by this channel is upon the solar zenith angle, backscattering angle, and also upon the size and orientation of the scanspot.

ACKNOWLEDGEMENTS

The authors wish to express their gratitude to the following agencies for supplying valuable data for this report: The Meteorological Services of Egypt, Turkey, Greece, and Libya, and the Meteorological Office Zurich Airport.

REFERENCES

Feigelson, E. M., M. S. Malkevich, S. Ya. Kogan, T. D. Koronatova, K. S. Glazova, and M. A. Kuznetsova, 1958: Calculation of the Brightness of Light, Translated from Russian. Consultants Bureau, Inc., New York, 1960.

Fritz, S. and J. Winston, 1962: Synoptic use of radiation measurements from satellite TIROS II, Mon. Wea. Rev., 90, 1-9.

_____, P. Krishna Rao, and M. Weinstein, 1964: Satellite measurements of reflected solar energy and energy received at the ground. J. atmos. Sci., 21, 141-151.

Fujita, T., 1962: A technique for precise analysis of satellite data; volume I - photogrammetry, MSL Report No. 14, U.S. Weather Bureau.

_____ 1964: The scanning printer and its application to detailed analysis of satellite radiation data, SMRP Research Paper No. 15, Univ. Chicago.

_____ 1963: Outline of a theory and examples for precise analysis of satellite radiation data, SMRP Research Paper No. 15, Univ. Chicago.

_____, T. Ushijima, W. Hass, G.T. Dellert, 1962: Meteorological interpretations of convective nephsystems appearing in TIROS cloud photographs, SMRP Research Paper No. 9, Univ. Chicago.

Hanel, R. A., W.R. Bandeen, B.T. Conrath, 1963: The infrared horizon of the planet earth, J. atmos. Sci., 20, 73-86.

Kuettner, J., 1959: The band structure of the atmosphere, Tellus, 11, 267-294.

NASA, 1962: TIROS IV radiation data catalog and user's manual, Goddard Space Flight Center, Greenbelt, Maryland.

Nordberg, W., W.R. Bandeen, B.J. Conrath, V. Kunde, and I. Persano, 1961: Preliminary results of radiation measurements from the TIROS III meteorological satellite, J. atmos. Sci., 19, Univ. Chicago.

Pedersen, F., and T. Fujita, 1963: Synoptic interpretation of TIROS III measurements of infrared radiation, SMRP Research Paper No. 19, Univ. Chicago.

Reiter, F.R., 1961: Meteorologie der Strahlstroeme, Springer Verlag, Wien.

Wark. D Q., G. Yamamoto, and J. H. Lienesch 1962: Methods of estimating infrared flux and surface temperature from meteorological satellites, J. atmos. Sci., 19, 369-384.

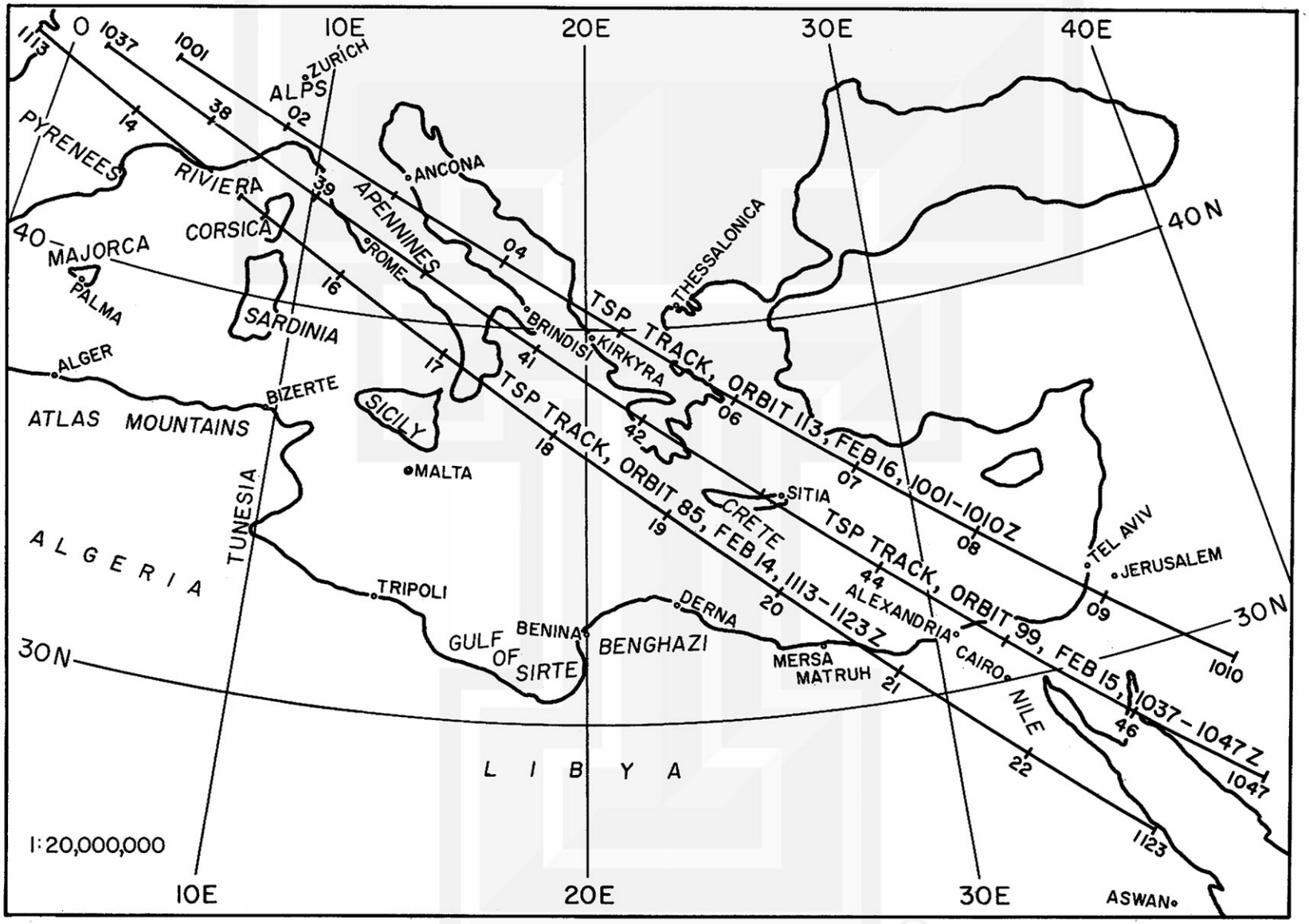

Fig. 1. The TSP tracks of Orbits 85, 99, and 113 used in this research. Places mentioned in the paper are also included.

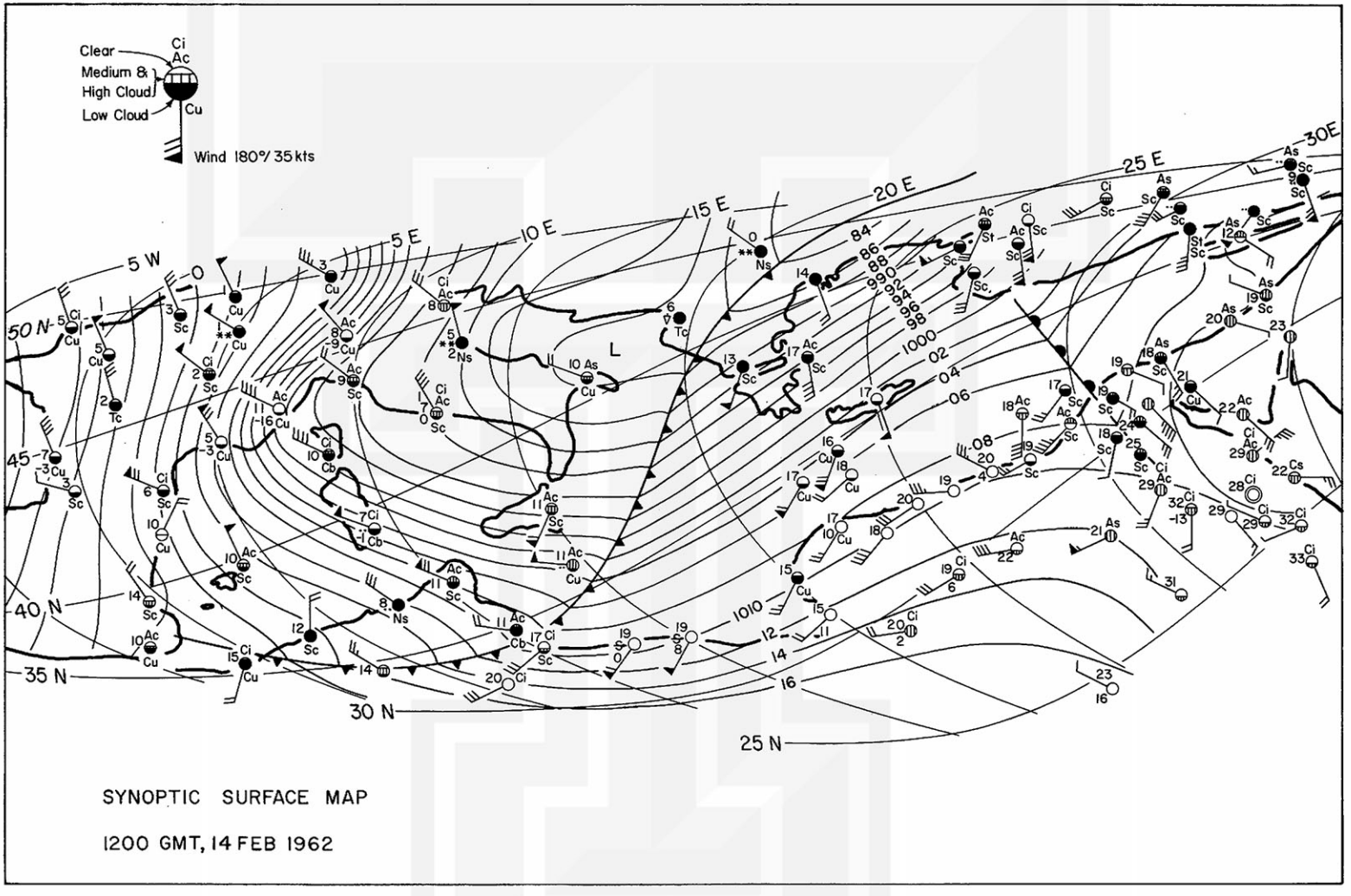

Fig. 2. Synoptic surface map at 1200 GMT 14 February 1962. Winds plotted with a long barb represent 5 kts, and with a flag, 25 kts. The cloud covers are represented within a station circle by painted and hatched areas which are proportional to the cloud covers below and above 2500 m, respectively. An example of the station model is shown in the upper left-hand corner.

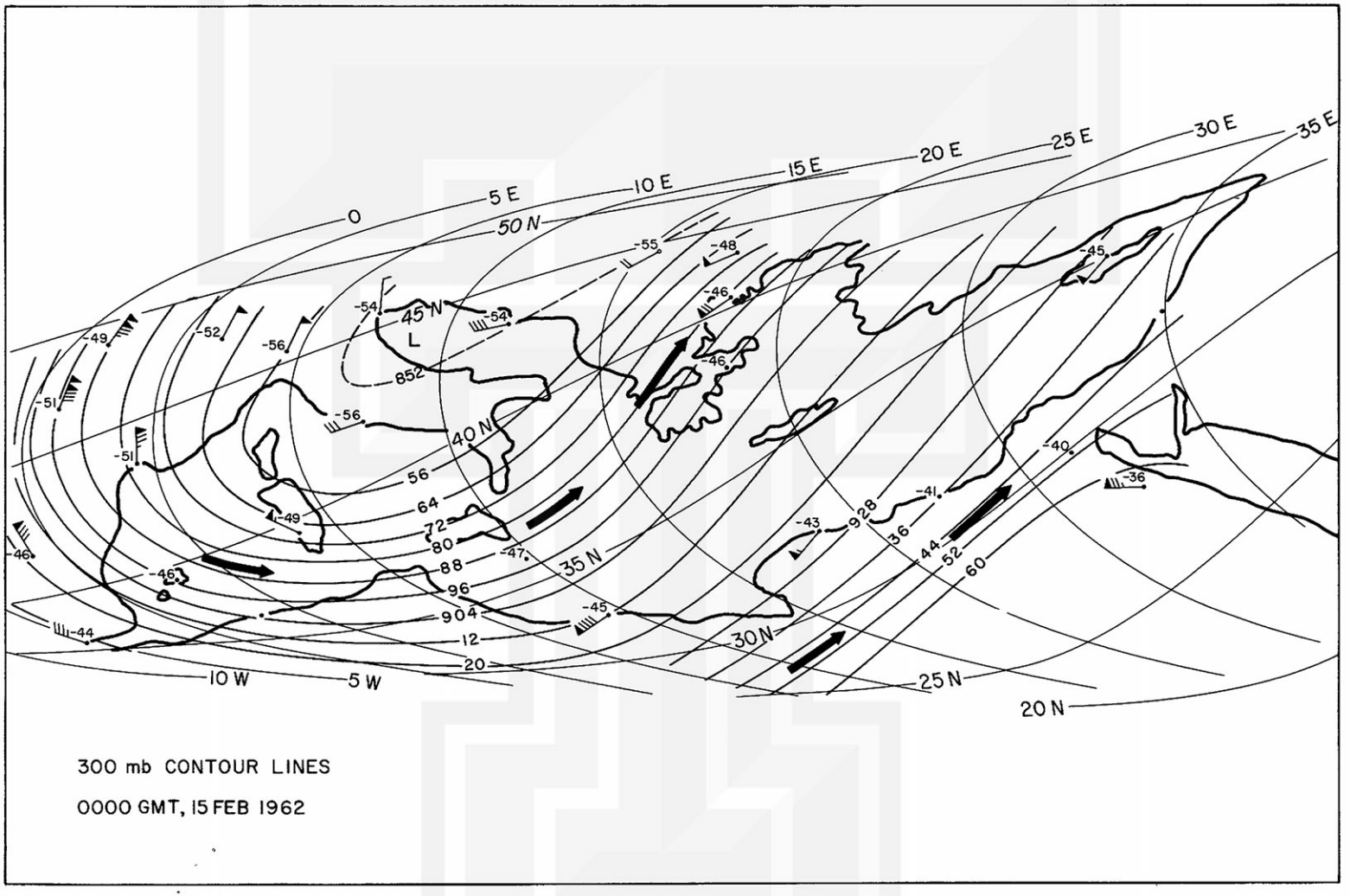

Fig. 3. 300-mb contour map (intervals 80 m) at 0000 GMT 15 February 1962. Regions of maximum winds are indicated by heavy arrows.

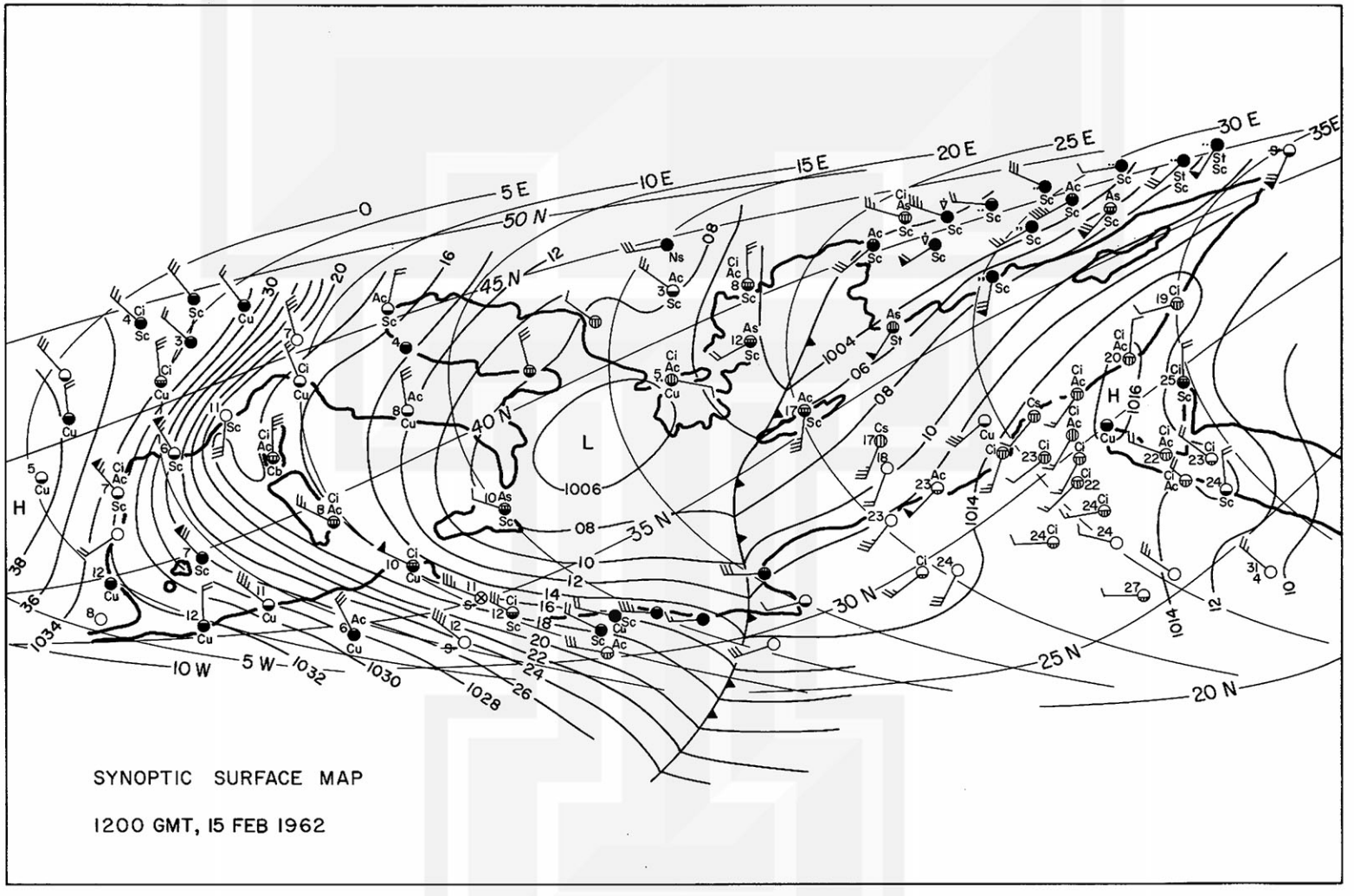

Fig. 4. Synoptic surface map at 1200 GMT 15 February 1962. Plotted symbols are the same as in Fig. 2.

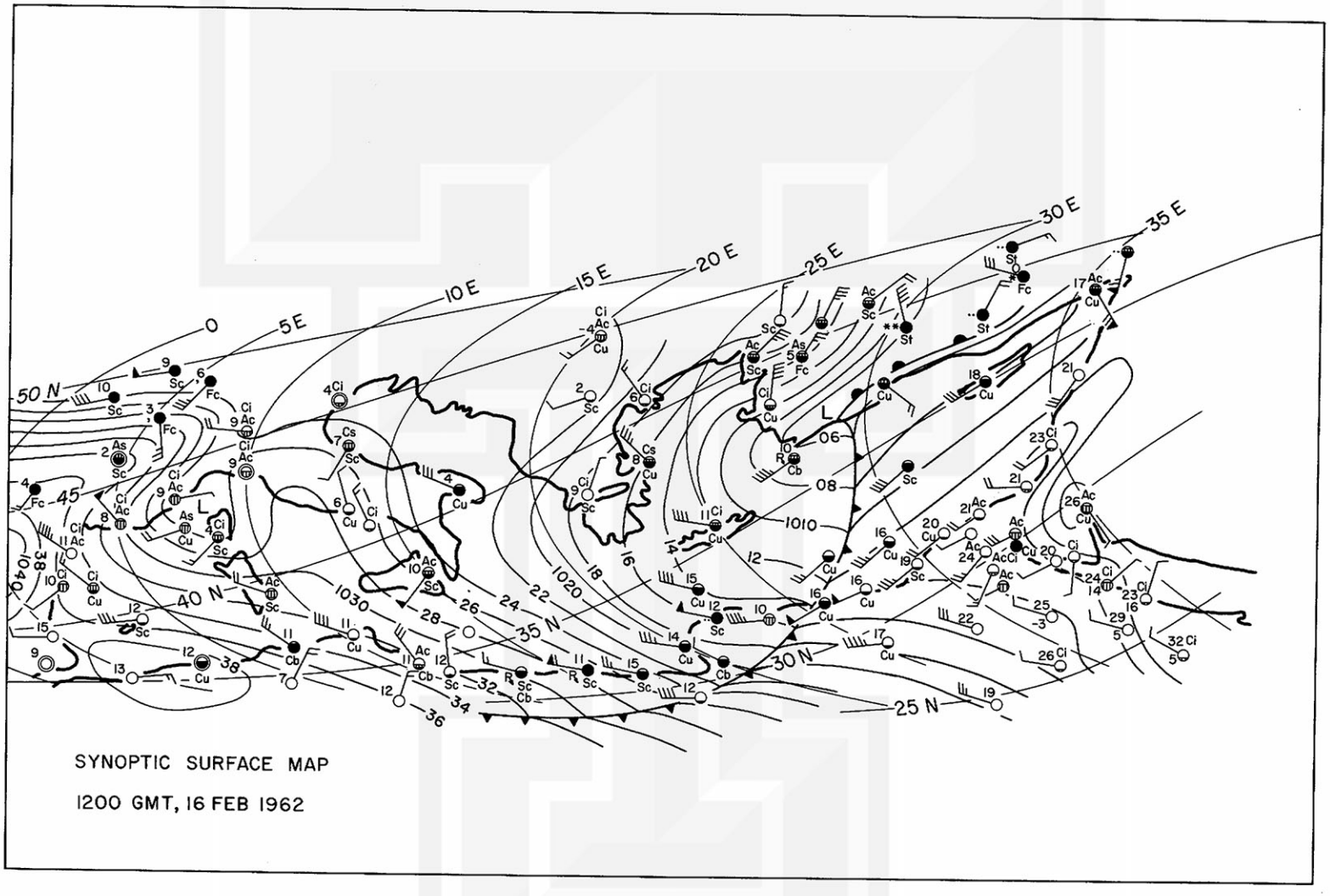

Fig. 5. Synoptic surface map at 1200 GMT 16 February 1962. Plotted symbols are the same as in Fig. 2.

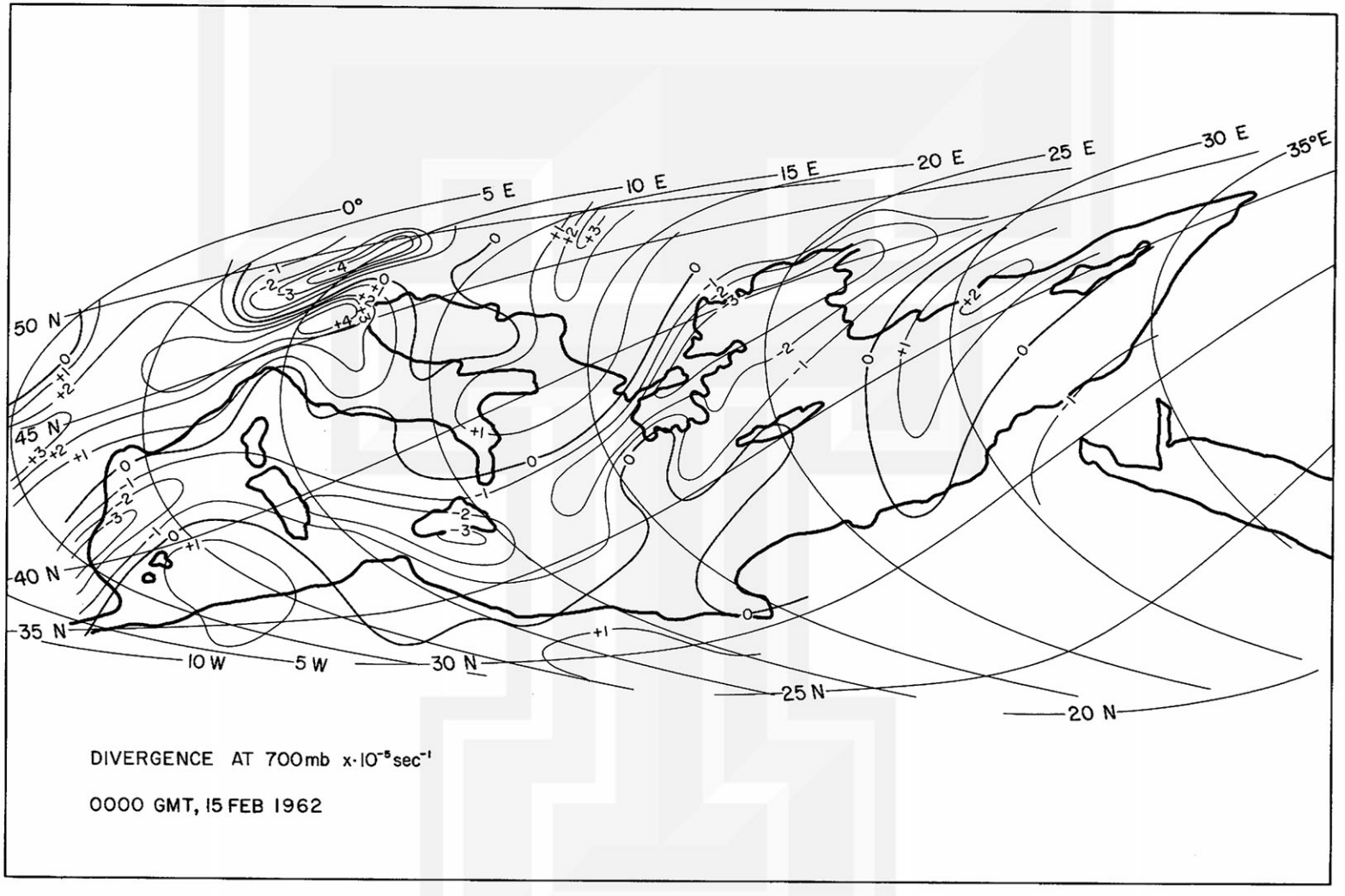

Fig. 6. Map showing the computed divergence (X 10^{-5} sec^{-1}) at 700-mb surface at 0000 GMT 15 February 1962. Negative values indicate convergence. Note the strong orographic influence of the Alps and the Pyrenees.

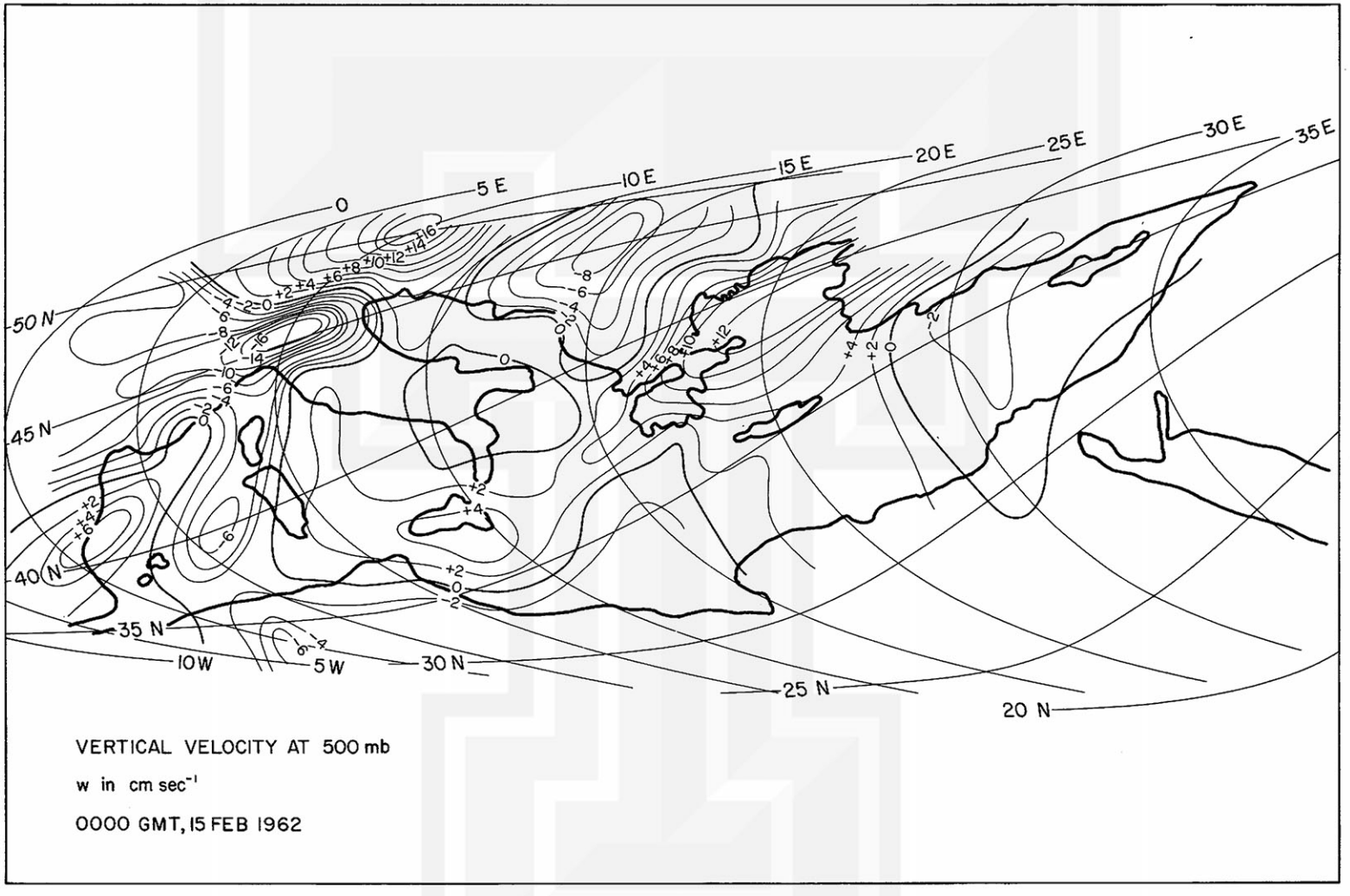

Fig. 7. Map showing the computed vertical velocity in cm sec^{-1} at the 500-mb surface at 0000 GMT 15 February 1962. Positive values indicate upward motion.

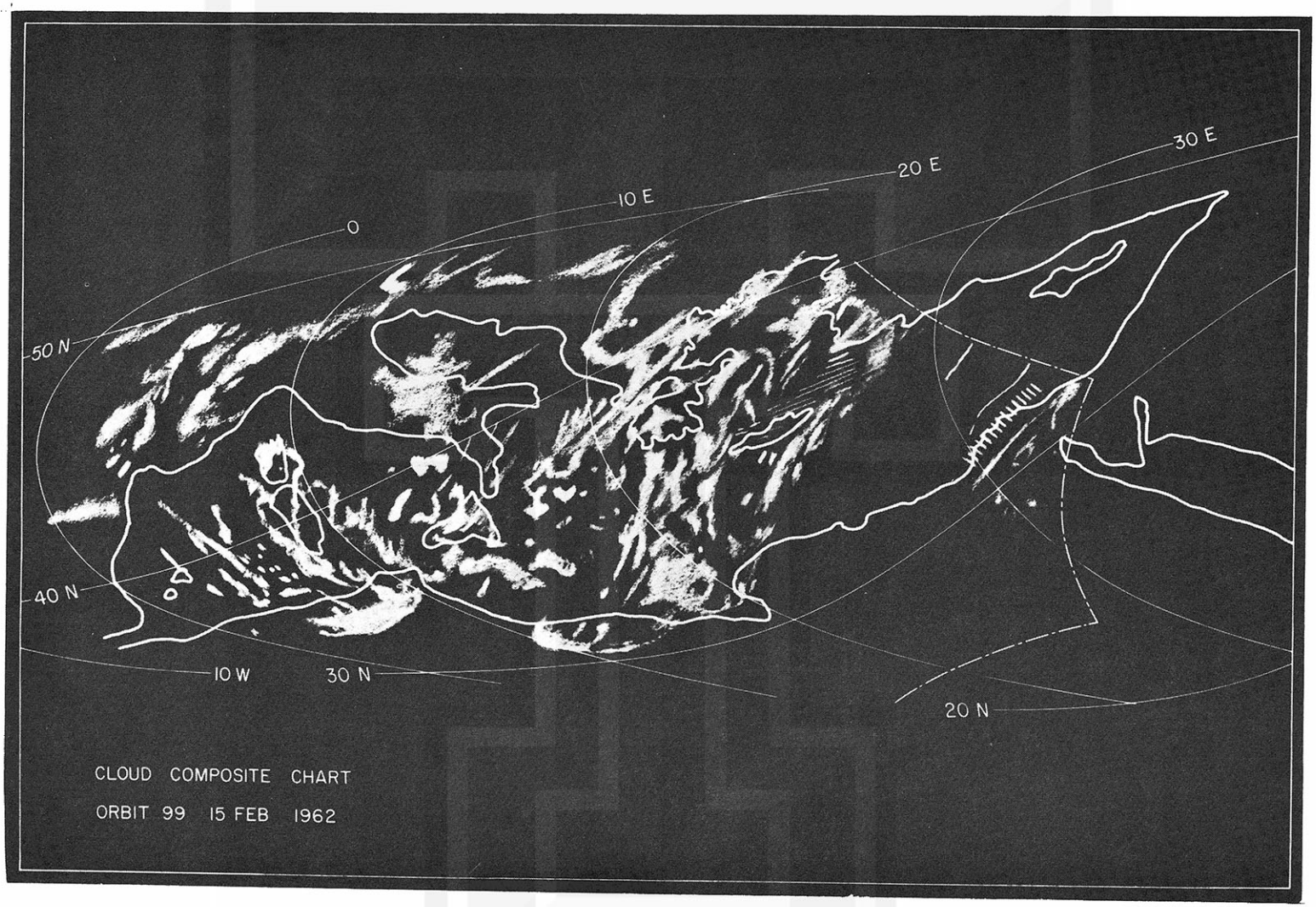

Fig. 8. Composite cloud map from Orbit 99, 15 February 1962. Note that the cloud bands over the western Mediterranean are oriented in the direction of low-level winds. Note also the wave clouds over Egypt and east of Crete.

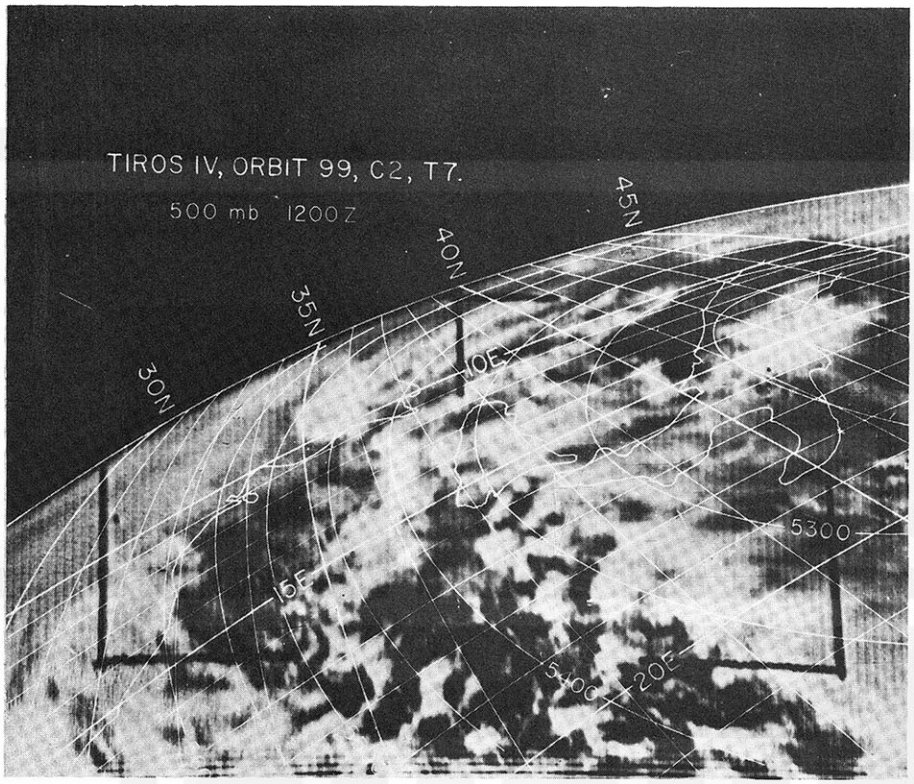

Fig. 9. Frame 7, Orbit 99, 15 February 1962, exposed at 10h 43m 12s, when the TSP was just east of Sitia in Crete. 500-mb contour lines (intervals 50 m) at 1200 GMT and coastlines are drawn on the picture. The cloudtops over Italy are sheared off.

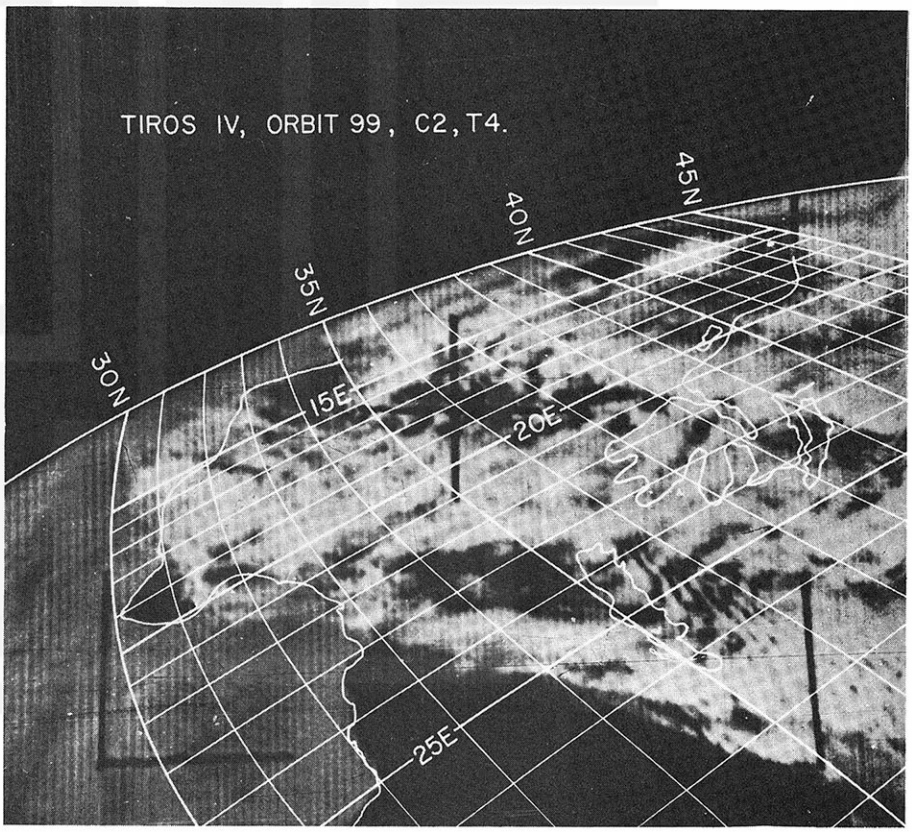

Fig. 10. Frame 4, Orbit 99, 15 February 1962, exposed at 10h 44m 42s when the TSP was off the Egyptian coast. Note the mountain wave clouds to the leeward side of Crete.

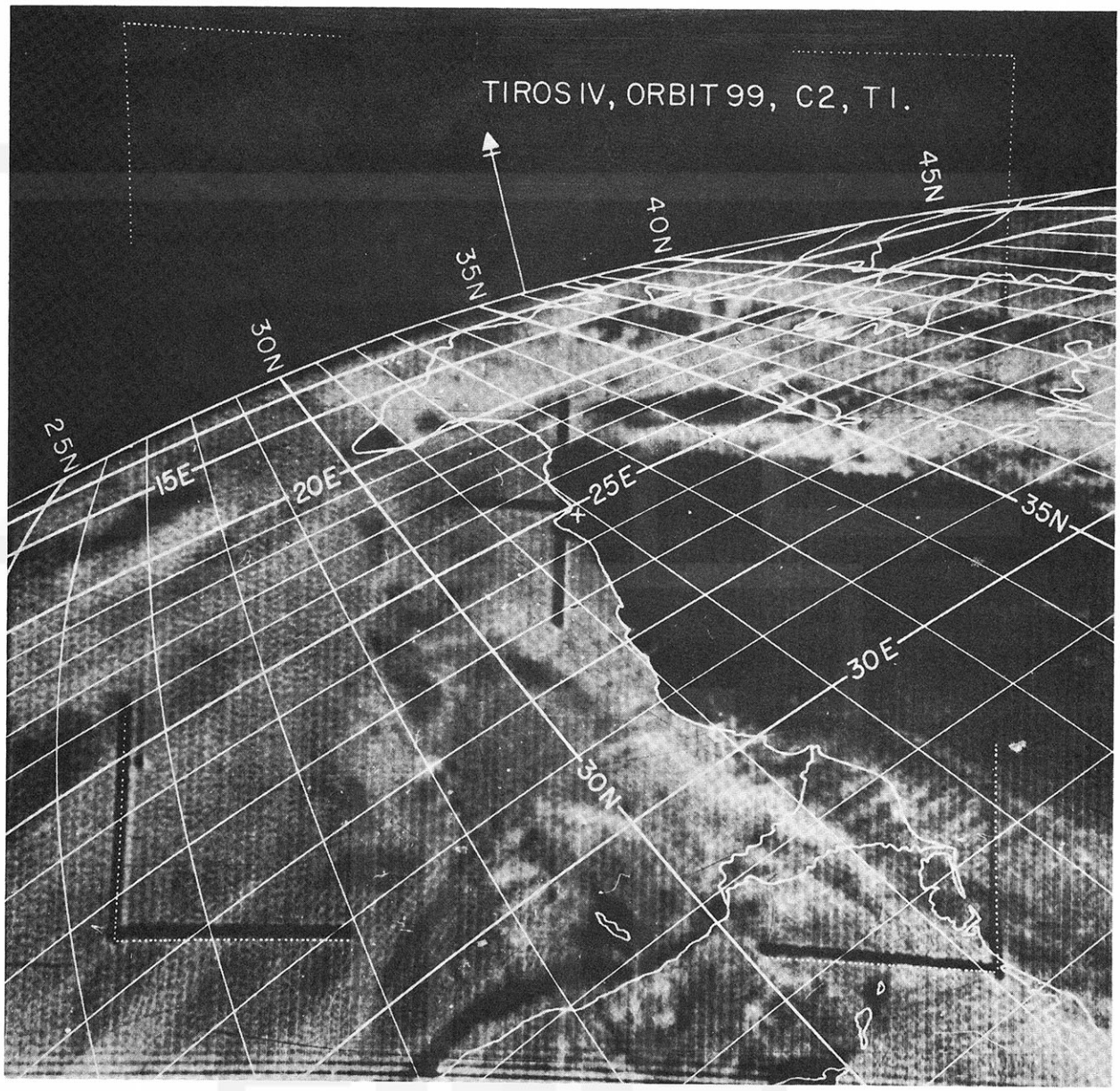

Fig. 11. Frame 1, Orbit 99, 15 February 1962, exposed at 10h 46m 12s when the TSP was just east of the Red Sea. The Libyan coastline and the Nile are clearly visible. The jet stream wave clouds over Egypt can also be seen.

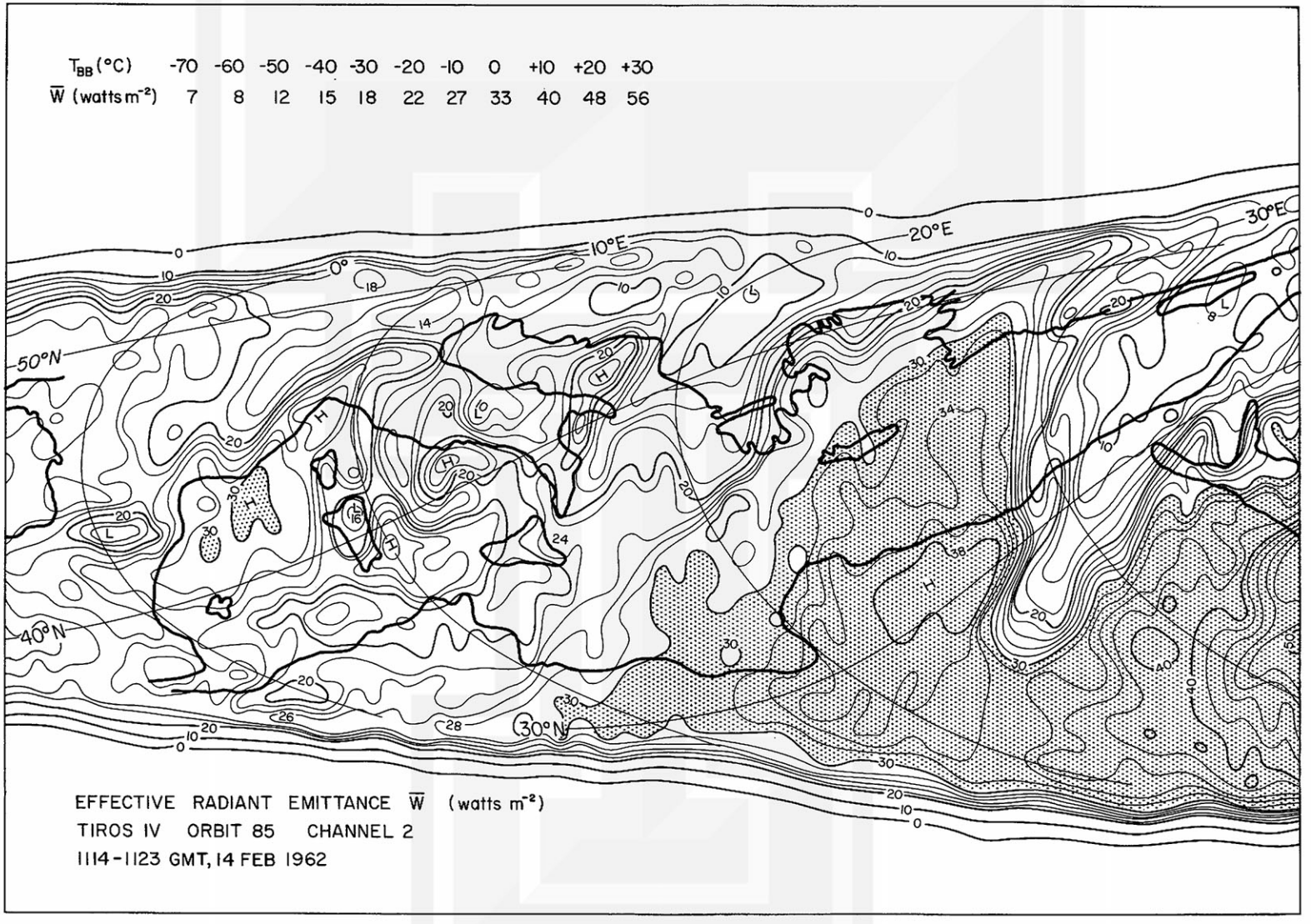

Fig. 12. Patterns of Channel 2 (8 - 12 μ) effective radiant emittance (watts m^{-2}) from TIROS IV, Orbit 85, 14 February 1962. Shown in the upper left is a table for obtaining equivalent blackbody temperatures from the effective radiant emittance. The stippled areas show radiation values above 30 watts m^{-2}. Longitude and latitude lines drawn for every 10^{0} interval and the coastlines are indicated by heavy lines.

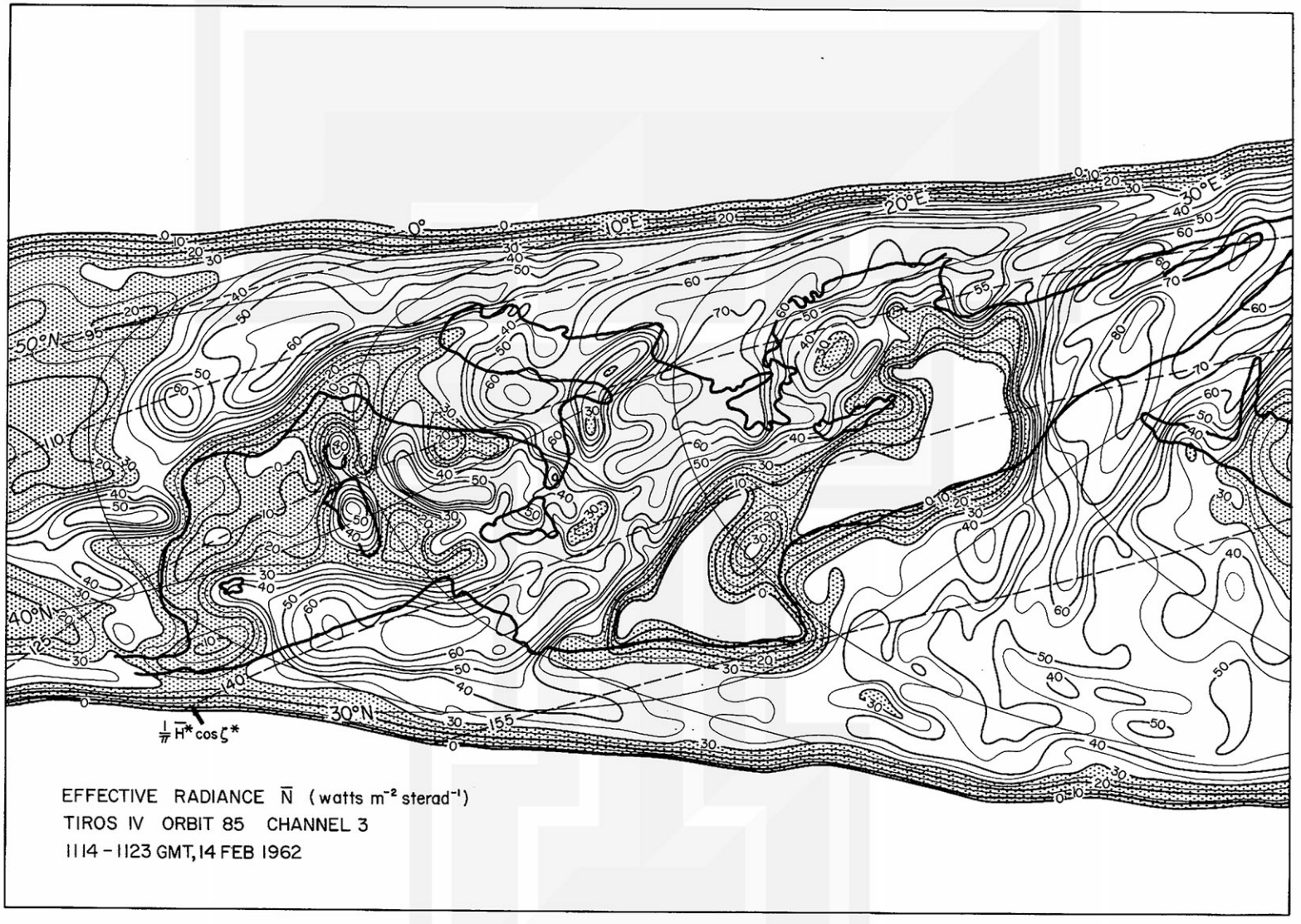

Fig. 13. Patterns of Channel 3 (0.25 - 6.0μ) effective radiance (watts m^{-2} $sterad^{-1}$) from TIROS IV, Orbit 85, 14 February 1962. The stippled areas show radiation values between 0 and 30 watts m^{-2} $sterad^{-1}$. Isolines for incoming extra-terrestrial effective solar radiation are indicated by dashed lines. Longitude and latitude lines are drawn for every 10^{o} interval and the coastlines are indicated by heavy lines.

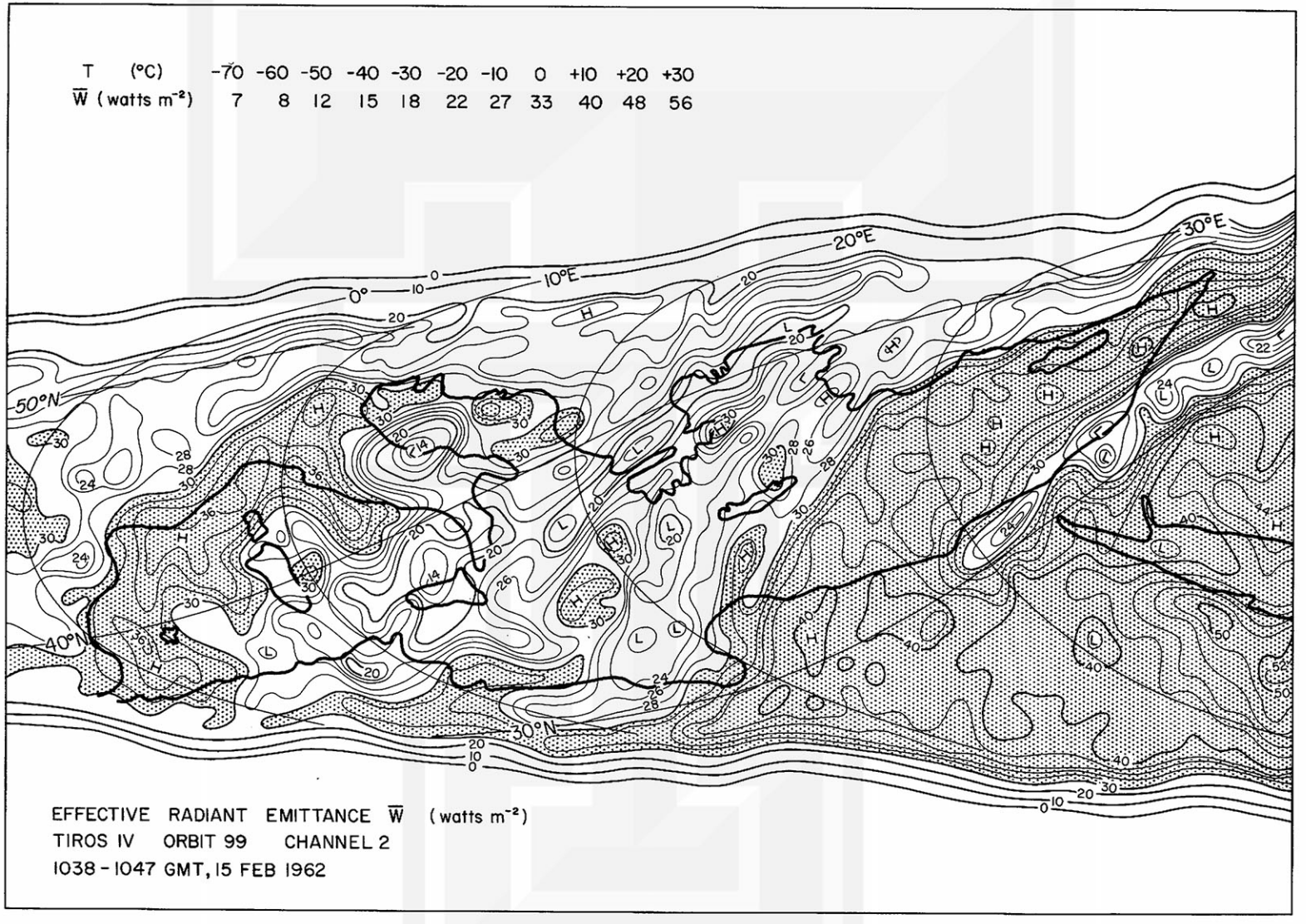

Fig. 14. Patterns of Channel 2 effective radiant emittance (watts m^{-2}) from TIROS IV, Orbit 99, 15 February 1962. (cf., Fig. 12).

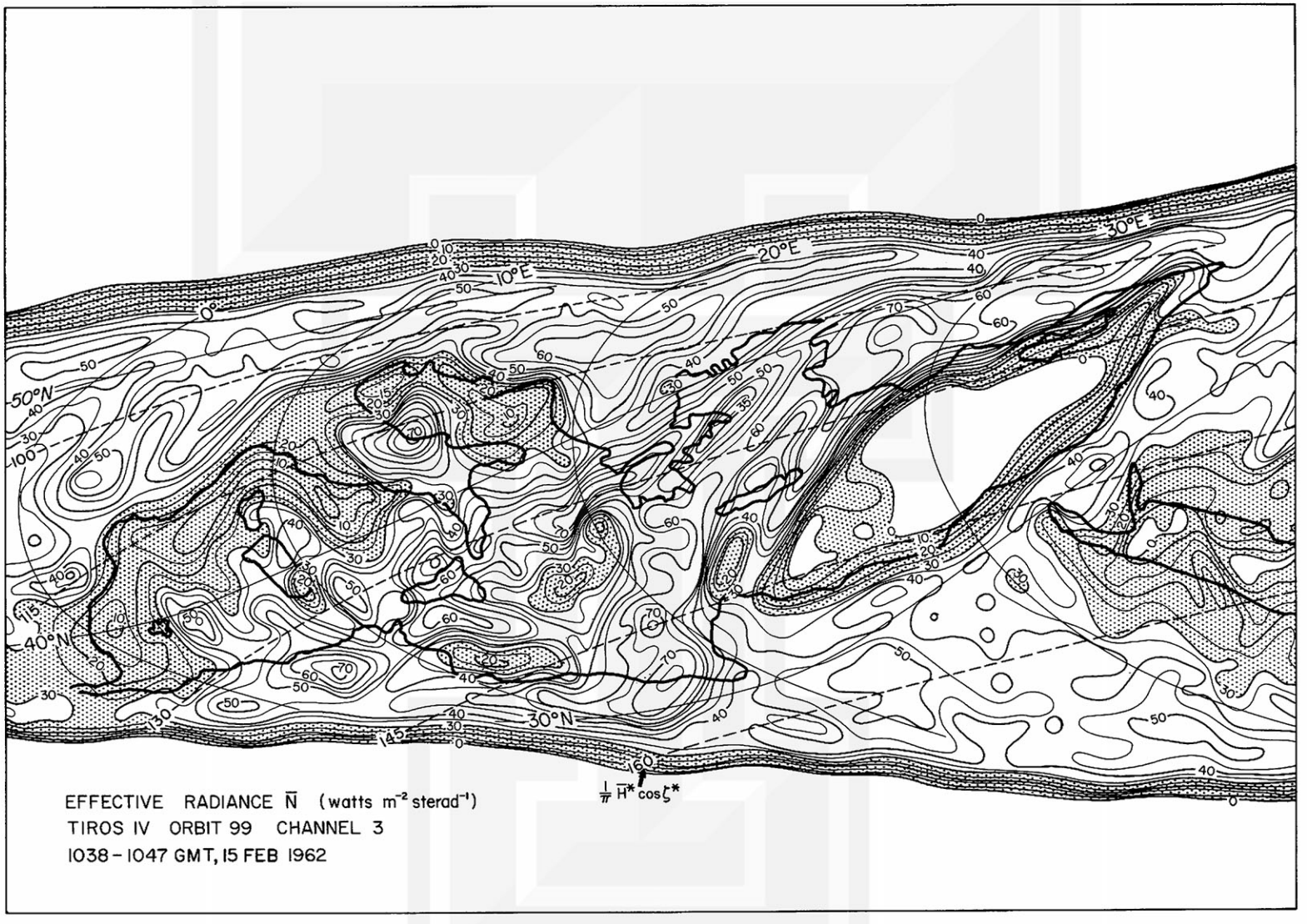

Fig. 15. Patterns of Channel 3 effective radiance (watts m^{-2} $sterad^{-1}$) from TIROS IV, Orbit 99, 15 February 1962. (cf., Fig. 13).

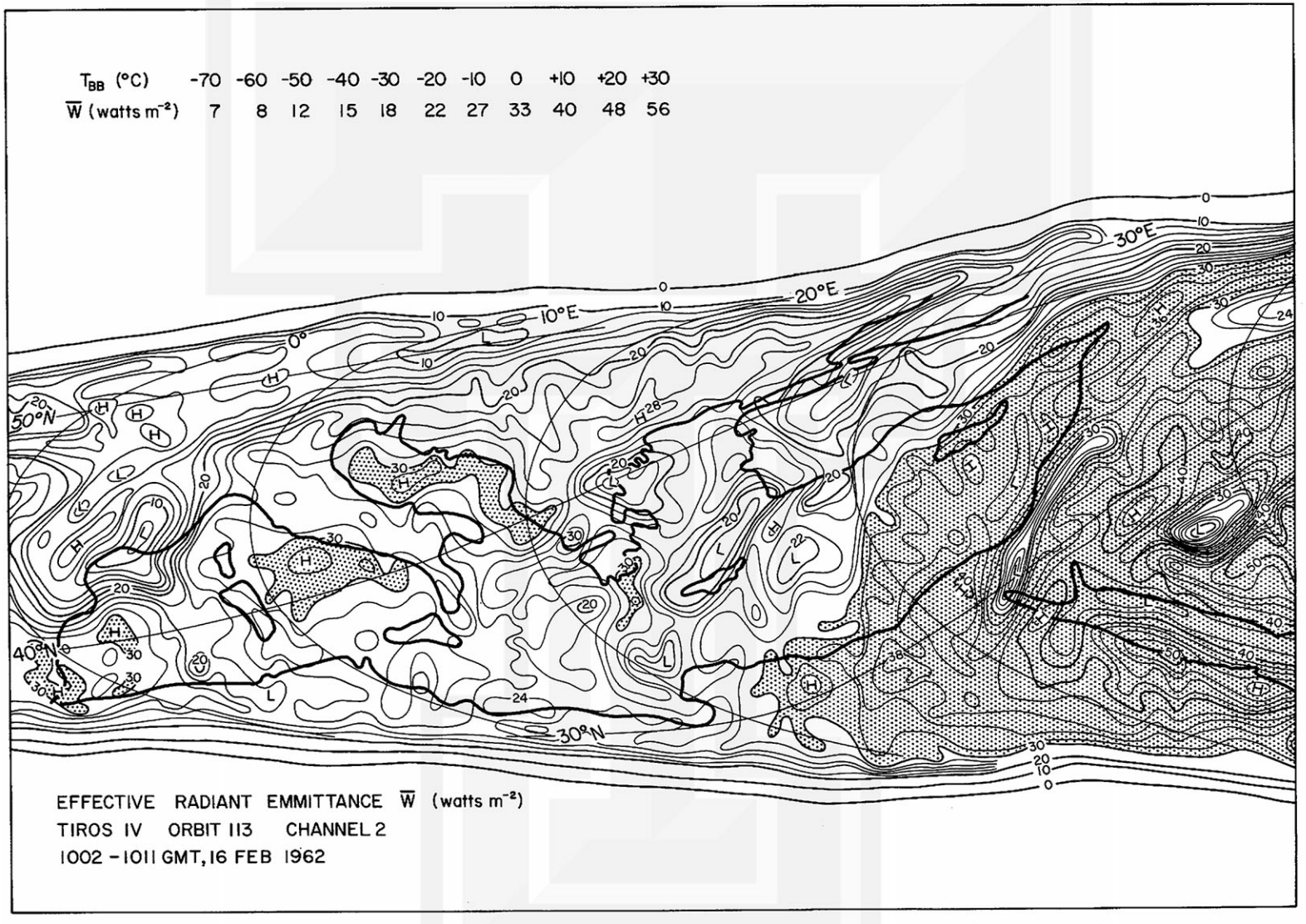

Fig. 16. Patterns of Channel 2 effective radiant emittance (watts m^{-2}) from TIROS IV, Orbit 113, 16 February 1962. (cf., Fig. 12).

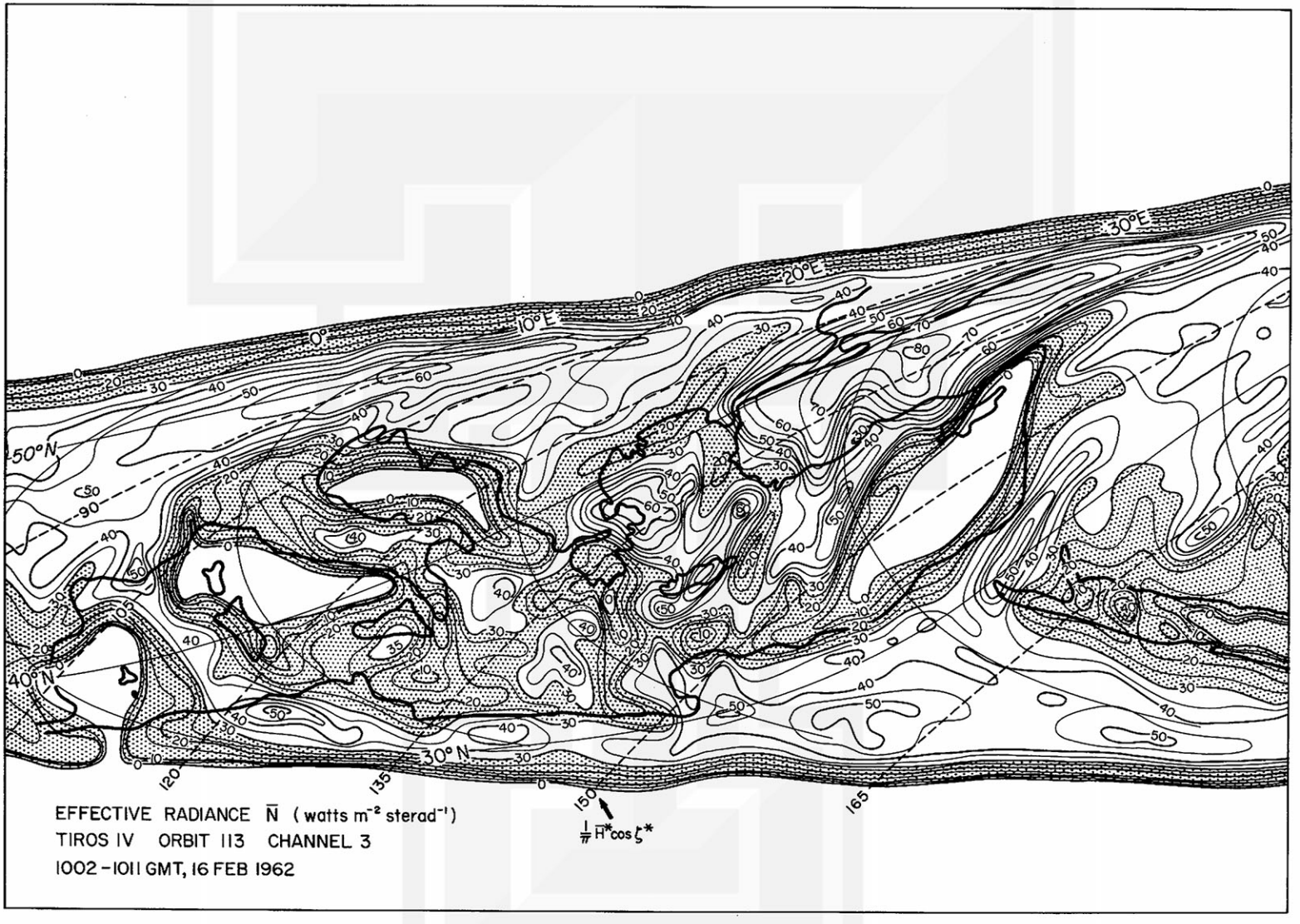

Fig. 17. Patterns of Channel 3 effective radiance (watts m^{-2} $sterad^{-1}$) from TIROS IV, Orbit 113, 16 February 1962. (cf., Fig. 13).

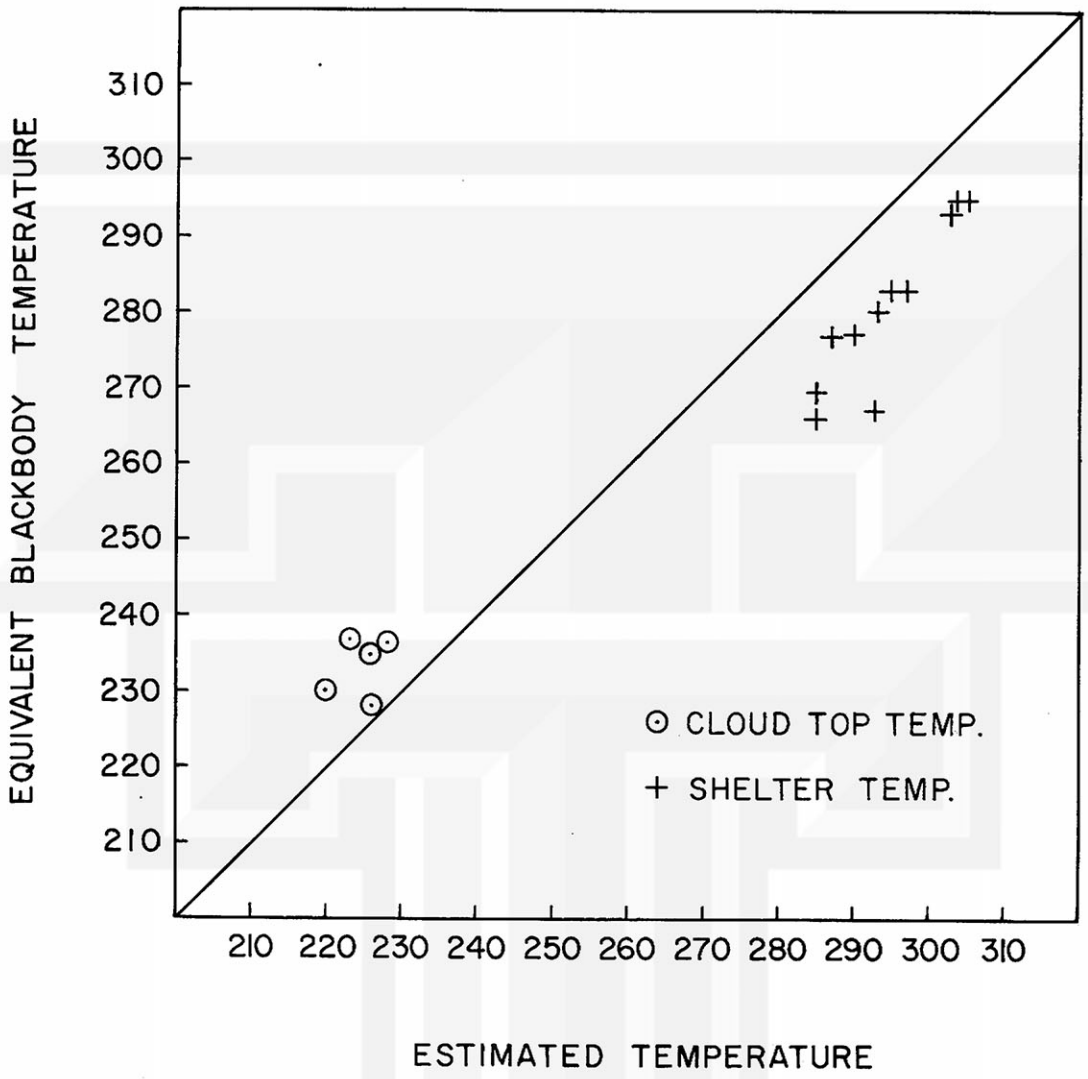

Fig. 18. Computed equivalent blackbody temperatures from Channel 2 compared with observed shelter temperatures and estimated cloud-top temperatures.

MESOMETEOROLOGY PROJECT - - - - - RESEARCH PAPERS

(Continued from front cover)

16. Preliminary Result of Analysis of the Cumulonimbus Cloud of April 21, 1961 -Tetsuya Fujita and James Arnold

17. A Technique for Precise Analysis of Satellite Photographs - Tetsuya Fujita

18. Evaluation of Limb Darkening from TIROS III Radiation Data - S.H.H. Larsen, Tetsuya Fujita, and W. L. Fletcher

19. Synoptic Interpretation of TIROS III Measurements of Infrared Radiation -Finn Pedersen and Tetsuya Fujita

20. TIROS III Measurements of Terrestrial Radiation and Reflected and Scattered Solar Radiation - S.H.H. Larsen, Tetsuya Fujita, and W.L. Fletcher

21. On the Low-level Structure of a Squall Line - Henry A. Brown

22. Thunderstorms and the Low-level Jet - William D. Bonner

23. The Mesoanalysis of an Organized Convective System - Henry A. Brown

24. Preliminary Radar and Photogrammetric Study of the Illinois Tornadoes of April 17 and 22, 1963 - Joseph L. Goldman and Tetsuya Fujita

25. Use of TIROS Pictures for Studies of the Internal Structure of Tropical Storms -Tetsuya Fujita with Rectified Pictures from TIROS I Orbit 125, R/O 128 -Toshimitsu Ushijima

26. An Experiment in the Determination of Geostrophic and Isallobaric Winds from NSSP Pressure Data - William Bonner

27. Proposed Mechanism of Hook Echo Formation - Tetsuya Fujita with a Preliminary Mesosynoptic Analysis of Tornado Cyclone Case of May 26, 1963 -Tetsuya Fujita and Robbi Stuhmer

28. The Decaying Stage of Hurricane Anna of July 1961 as Portrayed by TIROS Cloud Photographs and Infrared Radiation from the Top of the Storm -Tetsuya Fujita and James Arnold

29. A Technique for Precise Analysis of Satellite Data, Volume II - Radiation Analysis, Section 6. Fixed-Position Scanning - Tetsuya Fujita

30. Evaluation of Errors in the Graphical Rectification of Satellite Photographs -Tetsuya Fujita

(Continued on outside)

MESOMETEOROLOGY PROJECT - - - - - RESEARCH PAPERS

(Continued from inside)

31. Tables of Scan Nadir and Horizontal Angles - William Bonner

32. A Simplified Grid Technique for Determining Scan Lines Generated by the TIROS Scanning Radiometer - James Arnold

33. A Study of Cumulus Clouds Over the Flagstaff Research Network with the Use of U-2 Photographs - Dorothy L. Bradbury and Tetsuya Fujita

34. The Scanning Printer and Its Application to Detailed Analysis of Satellite Radiation Data - Tetsuya Fujita